Analysis of cloud-resolving simulations of a tropical mesoscale convective system observed during TWP-ICE: Vertical fluxes and draft properties in convective and stratiform regions

Agnieszka A. Mrowiec,[1,2] Catherine Rio,[3] Ann M. Fridlind,[2] Andrew S. Ackerman,[2] Anthony D. Del Genio,[2] Olivier M. Pauluis,[4] Adam C. Varble,[5] and Jiwen Fan[6]

[1]   We analyze three cloud-resolving model simulations of a strong convective event observed during the TWP-ICE campaign, differing in dynamical core, microphysical scheme or both. Based on simulated and observed radar reflectivity, simulations roughly reproduce observed convective and stratiform precipitating areas. To identify the characteristics of convective and stratiform drafts that are difficult to observe but relevant to climate model parameterization, independent vertical wind speed thresholds are calculated to capture 90% of total convective and stratiform updraft and downdraft mass fluxes. Convective updrafts are fairly consistent across simulations (likely owing to fixed large-scale forcings and surface conditions), except that hydrometeor loadings differ substantially. Convective downdraft and stratiform updraft and downdraft mass fluxes vary notably below the melting level, but share similar vertically uniform draft velocities despite differing hydrometeor loadings. All identified convective and stratiform downdrafts contain precipitation below ~10 km and nearly all updrafts are cloudy above the melting level. Cold pool properties diverge substantially in a manner that is consistent with convective downdraft mass flux differences below the melting level. Despite differences in hydrometeor loadings and cold pool properties, convective updraft and downdraft mass fluxes are linearly correlated with convective area, the ratio of ice in downdrafts to that in updrafts is ~0.5 independent of species, and the ratio of downdraft to updraft mass flux is ~0.5–0.6, which may represent a minimum evaporation efficiency under moist conditions. Hydrometeor loading in stratiform regions is found to be a fraction of hydrometeor loading in convective regions that ranges from ~10% (graupel) to ~90% (cloud ice). These findings may lead to improved convection parameterizations.

1. Introduction

[2]   Cloud processes involve a broad span of spatial and temporal scales, from fast small-scale turbulent motions to large-scale systems lasting days. Clouds also cover large portions of the Earth surface, impacting energy and water budgets, as well as transport of mass, momentum, moisture and heat. Understanding cloud-climate interactions therefore requires making connections between multi-scale cloud processes, their net impacts, and feedbacks that compose a global response to various perturbations.

[3]   General circulation models (GCM) do not have a fine enough grid mesh to explicitly simulate convective scales and must rely on parameterizations. Despite extensive knowledge of mesoscale convective system (MCS) structure and organization from observations, the effect of MCS internal circulations on the modification of the large-scale environment are still misrepresented in GCMs. Most convective parameterizations used in large-scale models focus on the convective-scale motions and neglect the mesoscale circulations associated with large convective systems [*Donner*, 1993], despite known importance of the mesoscale impacts on

[1]Center for Climate Systems Research, Columbia University, New York, New York, USA.
[2]NASA Goddard Institute for Space Studies, New York, New York, USA.
[3]Laboratoire de Meteorologie Dynamique, CNRS/IPSL, Paris, France.
[4]Courant Institute of Mathematical Sciences, New York University, New York, New York, USA.
[5]Department of Atmospheric Sciences, University of Utah, Salt Lake City, Utah, USA.
[6]Pacific Northwest National Laboratory, Richland, Washington, USA.

Corresponding author: A. A. Mrowiec, Center for Climate Systems Research, Columbia University, 2880 Broadway, New York, NY 10025, USA. (as3845@columbia.edu)

radiative, heat and water budgets [e.g., *Johnson*, 1984; *Houze*, 2004; *Frederick and Schumacher*, 2008].

[4] Improvement in the representation of cloud processes and cloud feedbacks is important for advancing climate forecasting skill [e.g., *Randall et al.*, 2003]. However, observations alone are often limited in providing 3D information on parameters currently used in large-scale parameterizations. Cloud resolving models (CRMs), which explicitly resolve the circulation within MCSs, have become an increasingly important tool used to link observations and parameterizations embedded in each atmospheric column of GCMs [e.g., *Arakawa and Xu*, 1992]. CRMs are not to be regarded as a substitute for observations, but rather they allow for detailed analysis and comparison with observations within idealized but still realistic scenarios, and have proven helpful to cloud parameterization development for GCMs [e.g., *Del Genio and Yao*, 1988; *Xu and Randall*, 1996; *Gray*, 2000; *Bretherton and Park*, 2009].

[5] Several studies, each based on a single CRM, have shown that some observed convective features may be well represented in CRMs [*Krueger*, 1988; *Xu and Randall*, 2000; *Gray*, 2000]. A number of CRM intercomparisons have been conducted in the framework of the Global Energy and Water Cycle Experiment (GEWEX) Cloud System Study (GCSS) program [e.g., *Redelsperger et al.*, 2000]. These intercomparisons have shown that CRMs are able to reproduce the general structure and propagation of tropical squall lines in reasonable agreement with observations. However, heating and moistening rates, even though qualitatively consistent, differ across models. Since CRM limitations arise in part from inadequate representation of microphysics and turbulence [*Guichard et al.*, 2004], using multiple CRMs may relieve some dependence of results on the formulation of any particular CRM. A recent CRM intercomparison presented in *Fridlind et al.* [2010, 2012], which used the Tropical Warm Pool International Cloud Experiment (TWP-ICE) campaign results [*May et al.*, 2008], involved evaluation of 13 CRM simulations against available observations of precipitation, latent heating rates, and radiative fluxes, as well as the general structure of the simulated MCS. In this paper we perform a more detailed analysis of 3 of those 13 simulations during the course of one convective event, with the objective of identifying robust cloud properties that may be later used to evaluate or improve convective parameterizations.

[6] A typical large convective system can be decomposed into two regions of precipitation: convective and stratiform [*Houze*, 2004]. In the convective region, strong updrafts carry warm, moist air from the boundary layer to the mid- and upper-troposphere, and convective downdrafts bring cooler, moist air down to the surface, all in the presence of heavy precipitation. Downdraft air, with low moist static energy, behaves as a density current; it spreads at the surface forming a cold pool immediately behind the gust front. A spreading cold pool produces a wake that can induce new convection formation at its edges [*Zipser*, 1977]. The long-lived stratiform region of a tropical MCS either trails the convective towers or it may surround them [*Mapes and Lin*, 2005], and is typically quite deep and spatially extensive (over 100 km characteristic size), much larger than the convective region. It is approximately horizontally uniform, and vertically layered, and consists of particles detrained from the convective tower [*Houze*, 1989]. This region is characterized not only by much weaker vertical motions and vertical mass fluxes but also with rather horizontally uniform precipitation that is weaker than the convective rain [*Zipser*, 1969].

[7] CRM intercomparisons have mostly focused on mean cloud system properties, averaged either over the total domain or over the cloudy area, but here we focus on an analysis of the properties of updrafts and downdrafts in the convective and stratiform regions and associated cold pools. The goal of this study is to compare the areal coverage of observed and simulated convective and stratiform regions and to investigate basic characteristics of the simulated structures. For this purpose, we focus on a strong mesoscale convective event that took place on the 23rd of January 2006 off the coast of Australia and was observed during the TWP-ICE campaign [*May et al.*, 2008]. We consider a subset of 3D CRM simulations presented in *Fridlind et al.* [2012] and partition the CRM domain into convective and stratiform regions consistent with observational analysis. Then, using the simulations, the structures within these regions are identified in order to analyze their properties and their contributions to the vertical transport of mass, heat and moisture. A similar approach was taken by *Gray* [2000], in which a single CRM was used to analyze a TOGA-COARE case. Here we identify degrees of consistency across differing CRMs for a TWP-ICE case. We use higher resolution simulations that include two-moment microphysics and an aerosol size distribution profile based on observations. Our conditional sampling of drafts also allows independently capturing 90% of mass transport by updrafts and downdrafts, as described below.

[8] The paper is organized as follows. Section 2 describes the observations and the simulations. In section 3 we discuss partitioning into stratiform and convective regions and comparison of the convective system's components among the simulations, including convective updrafts and downdrafts, stratiform updrafts and downdrafts and cold pools. In section 4 we discuss the relationship between updrafts and downdrafts in the convective region. Conclusions are summarized in section 5.

2. Observations and Simulations

[9] TWP-ICE was a multi-agency project centered on Darwin, Australia that was designed to improve our understanding of the factors controlling tropical convection. The experiment provided an extensive data set, including an array of In the 3-hourly soundings, as well as radar, satellite and in-situ measurements. A detailed description of experiment conditions, general climate, and measurements can be found in *May et al.* [2008]. This study focuses on the largest mesoscale convective system (MCS) that passed directly through the center of the TWP-ICE domain on January 23 − 24, dubbed "Landphoon John" by *May et al.* [2008] and event C in *Fridlind et al.* [2012].

[10] Multiple modeling studies and observational analyses have already drawn from the TWP-ICE data set. Using individual dynamics models, the properties of updrafts, entrainment processes, precipitation rates, and ice processes at cloud top have been studied by *Wang and Liu* [2009], *Wu et al.* [2009], *Zhang* [2009], *Del Genio and Wu* [2010] and *Wapler et al.* [2010]. An intercomparison of multiple

limited-area models (LAMs) run with nested grids over the duration of event C is presented in *Zhu et al.* [2012] and includes comparison with the ensemble presented in *Fridlind et al.* [2012]. Other studies focused on the sensitivity of microphysical and radiative processes to aerosol and ice nucleation formulation [*Fan et al.*, 2010; *Morrison and Grabowski*, 2011; *Zeng et al.*, 2011].

[11] Two CRMs are used in this analysis: the Distributed Hydrodynamic-Aerosol-Radiation Model Application (DHARMA) [*Stevens et al.*, 2002; *Ackerman et al.*, 2003], and the System for Atmospheric Modeling (SAM) [*Khairoutdinov and Randall*, 2003]. All three simulations, two using DHARMA and one using SAM, are part of the study described in *Fridlind et al.* [2012], and were run for 16 days (from January 18 to February 3 2006) on a similar domain (horizontally 192 km × 192 km for SAM and 176 km × 176 km for DHARMA), similar horizontal resolution (1000 m for SAM and ~900 m for DHARMA) and vertical resolution (stretched vertical grid 100–250 or 400 m in the troposphere), and both with periodic lateral boundary conditions and a model domain height of 24 km. Two of the three simulations were also analyzed in *Varble et al.* [2011]. Aside we note that some studies have shown that to correctly represent boundary-layer and convection interactions, a finer resolution of horizontal 200 m may be needed [*Petch et al.*, 2002; *Bryan et al.*, 2003; *Khairoutdinov et al.*, 2009].

[12] To allow for comparable development of the MCS (i.e. convective towers, stratiform anvils, cold pools) as realized over the experimental domain, a uniform set of initial conditions was used for all the simulations. Initial conditions at the beginning of the simulations (0Z January 18) were derived from the mean observed profiles of potential temperature and water vapor mixing ratio. The TWP-ICE experimental domain includes both land and ocean, but since the land plays a minimal role during the active monsoon period, the surface is idealized as marine. A uniform sea surface temperature was fixed at 29°C and the surface albedo was fixed at 0.07 in all shortwave bands. The models uniformly nudged mean horizontal winds above 500 m to the mean observed profiles with a two-hour timescale. The large-scale forcings were based on a variational analysis of observations [*Xie et al.*, 2010] and adopted at full strength below 15 km, linearly decreasing to zero strength at 16 km. Horizontally uniform nudging of mean water vapor and potential temperature above 15 km to mean observed profiles was applied with a six-hour timescale, which was necessary to maintain the observed structure of the upper troposphere [*Fridlind et al.*, 2010]. Since only 3-hour output was saved over 16-day simulations, here we also use 10-minute output over the event C time period obtained from restarts of each simulation.

[13] Both DHARMA and SAM solve the anelastic equations for deep convection, but they use different surface flux, sub-grid scale turbulence and radiative transfer schemes, and different dynamic cores. DHARMA uses second-order forward-in-time advection with third-order upwinding advection [*Stevens and Bretherton*, 1996], a Smagorinsky-Lilly turbulence closure, Monin-Obukhov similarity theory for surface fluxes, and 2-stream radiative transfer [*Toon et al.*, 1989]. SAM on the other hand uses advection computed with second-order finite differences in flux form with kinetic energy conservation and a third-order Adams-Bashforth time

integration scheme with variable time step length [*Khairoutdinov and Randall*, 2003], second-order momentum advection and monotonic positive-definite scalar advection in flux form with variable time step length [*Smolarkiewicz and Grabowski*, 1990], a Smagorinsky-type closure, the NCAR Community Atmospheric Model version 3.5 [*Collins et al.*, 1997] surface formulation, and a radiative scheme based on NCAR Community Climate Model (CAM3) [*Kiehl et al.*, 1998]. Additional details are provided in *Varble et al.* [2011].

[14] Simulations use one- or two-moment microphysics. The first DHARMA configuration (which we will call D1) uses a one-moment microphysical scheme that predicts the mass mixing ratios of four hydrometeor variables: cloud water, rain, combined cloud ice and snow, and graupel [*Grabowski*, 1999]. The division between the cloud ice and snow is diagnostic. D1 and the second DHARMA configuration (D2) use the same dynamical core but very different microphysics schemes, so that in the following we surmise that any substantial differences between DHARMA runs are entirely attributable to microphysics. In contrast, D2 and SAM (S2) use very different dynamical cores but rather similar microphysics schemes, both based on the 2-moment, 5-class scheme of *Morrison et al.* [2009] that predicts ten prognostic hydrometeor variables: the mass mixing ratios and number concentrations of cloud water, rain, cloud ice, snow, and graupel or hail. Both D2 and S2 used a trimodal aerosol profile derived from observations [*Fridlind et al.*, 2010]. However, there are some substantial differences between D2 and S2 microphysics. S2 uses a time invariant vertical aerosol profile whereas D2 uses an aerosol field that evolves, including consumption, transport, and nudging of the mean profile toward initial conditions with a 6-hour timescale [*Fridlind et al.*, 2012]. This alone drives substantially reduced cloud droplet concentrations in D2 relative to S2. S2 also treats dense ice as hail, using the fall speed expression and density of *Matson and Huggins* [1980], whereas D2 follows *Morrison et al.* [2009] in treating dense ice as slower-falling graupel. This alone drives a substantially greater loading of dense ice in D2 relative to S2. Other differences include the treatments of condensational adjustment, raindrop breakup, and heterogeneous ice nucleation in deposition and condensation modes. Because of these many differences in the 2-moment microphysics schemes used in SAM and DHARMA, in the following we cannot generally surmise that differences between S2 and D2 simulations are attributable only, or even primarily, to differences in their dynamical cores.

3. Convective and Stratiform Updraft and Downdraft Properties

3.1. Convective-Stratiform Partitioning

[15] The convective and stratiform regions of a mesoscale convective system differ from each other in terms of heating budget, precipitation amount and intensity, and spatial extent [*Houze*, 1982, 1989, 1997; *Johnson*, 1984]. There are a number of studies dedicated to classification of stratiform and convective precipitation based on different techniques. Many use the rain rate as a threshold parameter, or rain rate combined with cloud water content and/or vertical velocity [*Lang et al.*, 2003], strength of the updrafts and downdrafts [*Atlas et al.*, 2000], or using raindrop size distributions from
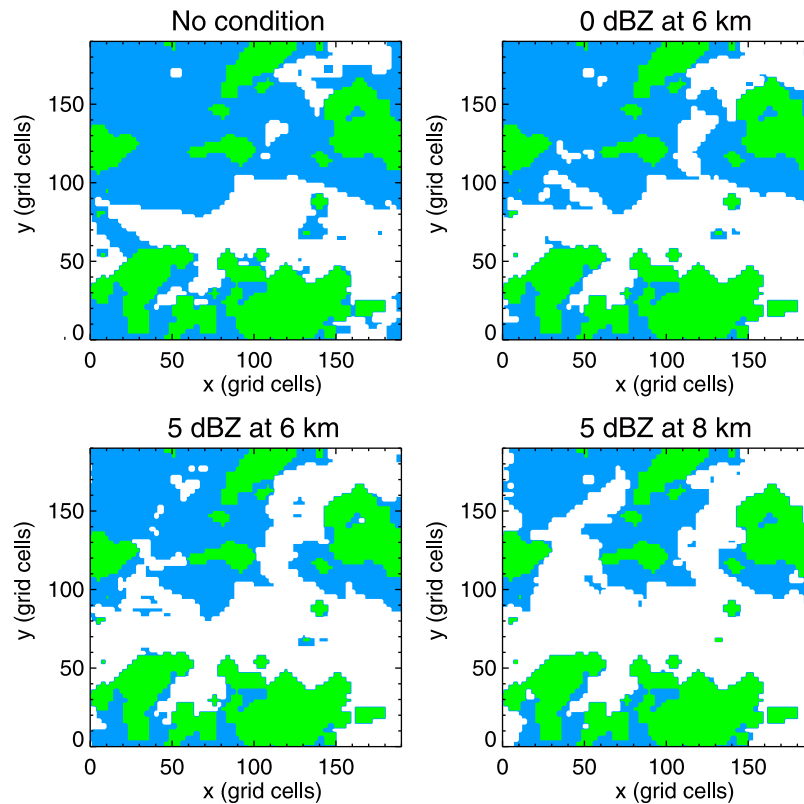
Figure 1. Examples of precipitation classification over a simulated radar reflectivity field in simulation D1. Green areas represent convective regions and blue areas represent the stratiform regions. Four panels show results with and without the upper-level conditions in the identification of stratiform regions (see text).

surface disdrometer measurements [*Tokay and Short*, 1996]. In this study we start with the *Steiner et al.* [1995] algorithm, which was designed to partition observations based on radar reflectivity and, in particular, to define the stratiform region. Based only on reflectivity, it was applied identically to both observations and simulation results. Retrievals of precipitation rate were observed from the C-band polarimetric scanning radar (CPOL) based on the algorithm in *Bringi et al.* [2009]. A description of this instrument can be found in *Keenan et al.* [1998].

[16] The Steiner method consists of a three-step algorithm applied to the gridded radar reflectivity field at an elevation below the melting level. All points with reflectivity exceeding 40 dBZ are first identified as convective. Any grid point not identified as convective in the first step, but which has reflectivity larger than the average (over a surrounding background area of 11 km radius) by at least a locally dependent threshold value is also identified as convective. This threshold value is constant for background reflectivity (Z_{BG}) less than 0, depends on the background reflectivity as $10 - Z_{BG}^2/180$ for $0 \le Z_{BG} < 42.43$ dBZ, and is 0 for $Z_{BG} \ge 42.43$ dBZ. All remaining rainy areas with radar echos above the observational detection limit (0 dBZ) are then identified as stratiform. Like any classification, such a method of partitioning may have disadvantages [*Tao and Simpson*, 1989]. Convective-scale updrafts may be tilted, so that they enter the stratiform region in upper levels, leading to areas of ascent below the stratiform column,

below the melting line. However, the *Steiner et al.* [1995] approach has the advantage of having been developed through extensive testing in the Darwin region to which we apply it here. It has also received wide use in the community [e.g., *Frederick and Schumacher*, 2008; *Holder et al.*, 2008].

[17] In order to apply the partitioning to model output, Rayleigh radar reflectivity is calculated at 2.5 km altitude for each simulation. It is computed using the sixth moment of the melted equivalent diameter size distribution, with a dielectric factor for all available ice hydrometeors of 0.208 [*Smith*, 1984]. In this study we also use a condition on reflectivity at 6 km to identify a column as stratiform. Without such a condition, the stratiform regions identified from the observations are consistently deep, but in the simulations the regions identified as stratiform sometimes included regions of notably shallower clouds. To compare simulations with observations, since the horizontal resolution of the measurement (2.5 km) was coarser than the grid spacing in the simulations (~1 km), and the partitioning method is sensitive to horizontal resolution [*Steiner et al.*, 1995], the resolution of simulated reflectivity was degraded to match the observations in a manner that conserves total reflectivity and interpolated vertically to 2.5 km and 6 km. Figure 1 compares stratiform areas identified in D1 with no upper level condition, and with the condition that radar reflectivity exceed 0 dBZ at 6 km, 5 dBZ at 6 km and 5 dBZ at 8 km. To avoid the possible misclassification of shallow convection, we arbitrarily chose to apply the condition of 5 dBZ at 6 km in
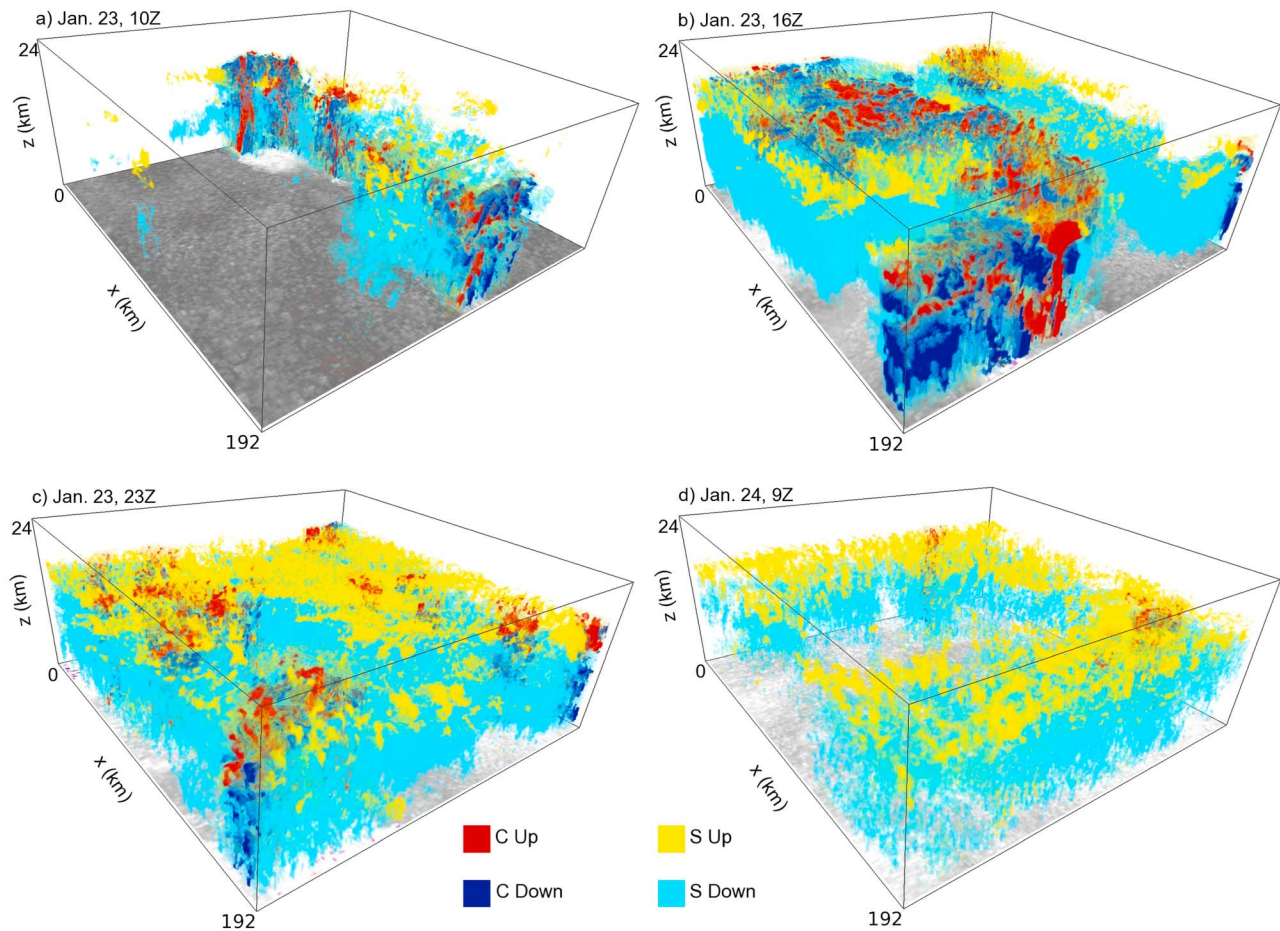
Figure 2. Examples of updrafts and downdrafts in stratiform and convective regions in simulation S2. Four stages of development of event C are shown: (a) onset, (b) peak of convective activity, (c) peak of stratiform activity, and (d) decay phase. Red and navy colors mark the convective updrafts and downdrafts respectively. Yellow and light blue mark stratiform updrafts and downdrafts respectively. At the surface white denotes cold pools and dark gray denotes warm spots in terms of equivalent potential temperature.

both observations and simulation. We note that the stratiform region identification has no effect on the convective region identification, which is independently applied first. Stratiform statistics are expected to better represent deep stratiform area when any of the 6- or 8-km thresholds are applied but general conclusions are not expected to be very sensitive to which one is used (see also discussion in *Fridlind et al.* [2012, Appendix A]).

[18] Examples of partitioning applied to S2 are shown in Figure 2, near the beginning of the convective event C, at the peak of the convective activity, during fully developed stratiform region and during the decay phase. Updrafts and downdrafts are shown as defined in the next section. In the intensifying stage of event C there is very little stratiform coverage. During the peak of the event, nearly the entire domain is precipitating. Visible cold pools associated with convective downdrafts cool the surface over the duration of the event. This visualization is only meant to give a qualitative impression of the partitioning.

[19] The results of partitioning of both observed and simulated reflectivity fields for the entire active monsoon period and the rain rate for all simulations are shown in Figure 3. The simulations reproduce the observed rain rate quite well,

both in terms of timing and amplitude (Figure 3a), which is to be expected because the meteorological forcing is derived from the observed rain rates [see *Fridlind et al.*, 2012]. As shown in *Varble et al.* [2011], even though the overall precipitation averaged over the model domains closely follows the observed precipitation, when the rainfall is partitioned into stratiform and convective regions separately, it may be overestimated in the former and underestimated in the latter region. For each of the large convective rain events, the simulations reproduce the buildup phase of convective area better than the decay (Figure 3b). After the peak, the convective coverage is overestimated by about 5%–20%. This delayed overproduction of the convective region likely results in part from cyclic boundary conditions: the convection must decay within the domain, whereas observed systems advect in and out of the domain [see *Varble et al.*, 2011]. Representation of stratiform regions (Figure 3c) is much more variable than the convective regions in the simulations. The stratiform regions are sometimes overestimated by as much as 50% during the first half of the active monsoon period in D2 and S2. The sometimes large difference in stratiform area between D1 and the two other simulations is attributable in part to the fact that the two-
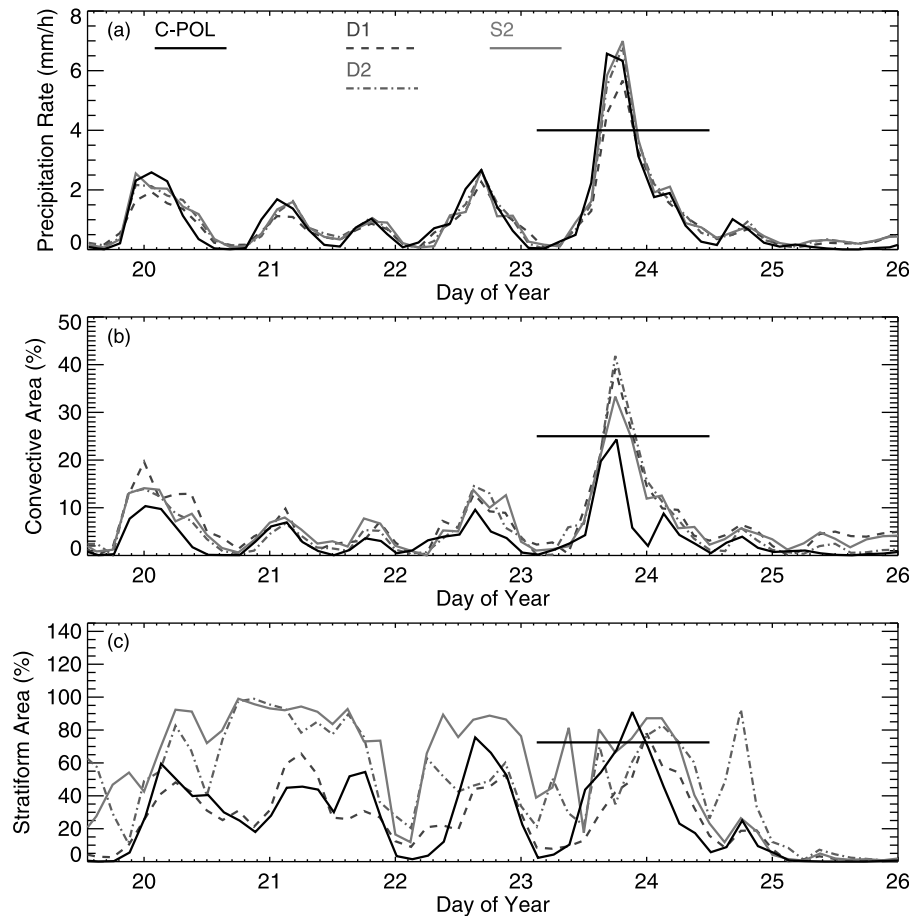
Figure 3. (a) Time series of rain rate near the surface, (b) convective area, and (c) stratiform area of the active monsoon period during TWP-ICE. Observations shown as solid lines and results for D1, D2 and S2 are shown by dashed, dash-dotted, and dash-triple-dotted lines respectively. Extent of event C is shown with horizontal lines.

moment scheme generally produces larger ice particles for a given snow mass mixing ratio, so a reflectivity of 5 dBZ aloft is more common as shown in *Varble et al.* [2011, Figure 18]. We note that this difference is sensitive to the partitioning approach, although differences are less pronounced during event C than earlier. During event C all three simulations match the observations more closely in terms of amplitude. The peak in stratiform areal coverage during the simulated event C in D2 and S2 is around 2–3 Z on January 24, which typically follows the convective maximum with a lag of several hours [*Mapes and Lin*, 2005], as the convective towers decay and transform into stratiform regions.

3.2. Updraft and Downdraft Identification

[20] The structural elements of an MCS have been found to include convective-scale updrafts and downdrafts [e.g., *Houze*, 1977; *Johnson*, 1976], a mesoscale updraft occurring in the stratiform ice region [e.g., *Brown*, 1979; *Houze*, 1989], and mesoscale downdraft that is present below the melting level in the stratiform anvil [e.g., *Zipser*, 1969, 1977]. As different definitions have been used to distinguish drafts, here we first describe them briefly and then focus on their properties.

[21] Parameterizations of deep convection often rely on mass-flux closure, in which a model grid cell is decomposed into three parts: an updraft ascending from cloud base to cloud top covering a small fraction of the domain compensated by both a downdraft which is part of the convective system and slow subsidence of the environment. In GCMs, it is assumed that above the boundary layer most of the vertical transport of mass, heat and moisture is carried out by updrafts and downdrafts [e.g., *Del Genio and Yao*, 1988; *Stensrud*, 2007, chapter 6.4.1]. Here, we assume that CRMs resolve the updrafts and downdrafts, and we neglect the known issue of gravity waves [e.g. *Xu et al.*, 2002], which will be addressed in future work. As our goal is to compare the circulation by three CRM configurations, identification of updrafts and downdrafts using a threshold on vertical velocity is considered sufficient to first order and will allow a direct comparison with previous studies using observations and modeling.

[22] In studies based on aircraft observations [*LeMone and Zipser*, 1980; *Zipser and LeMone*, 1980; *Lucas et al.*, 1994; *Jorgensen and LeMone*, 1989; *Igau et al.*, 1999] updrafts and downdrafts are typically identified using vertical velocity thresholds (w_{tr}) such as $|w| > w_{tr} = 0.5$ m s^{-1}. Often convective cores are additionally required to have a positive
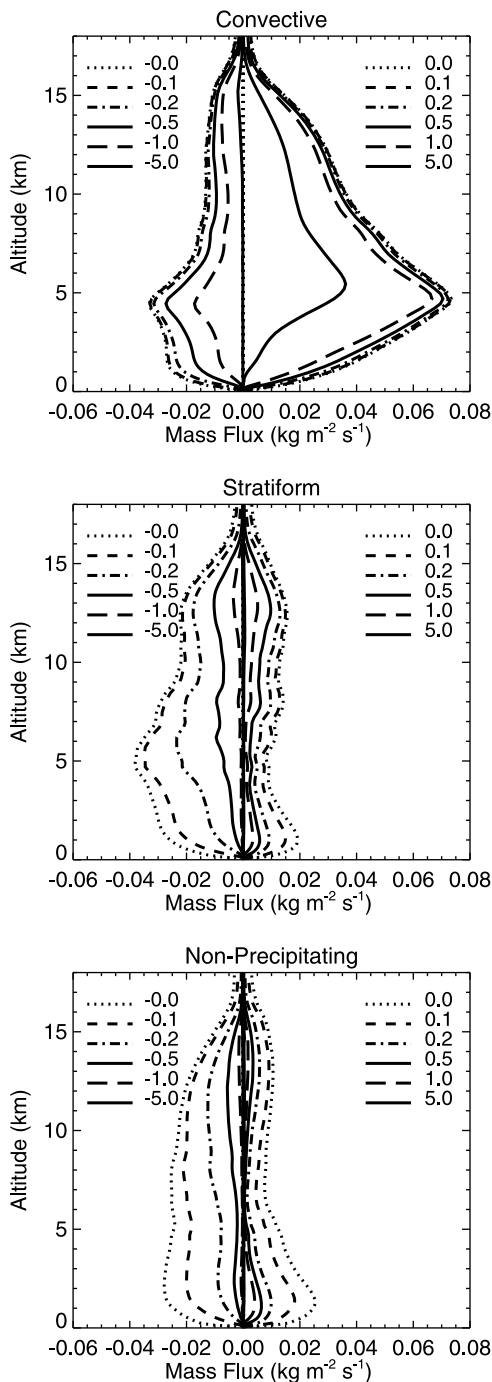
Figure 4. Vertical profiles of mass flux averaged over the domain during event C shown for D1 simulations with five thresholds on positive and negative vertical wind speeds (in units of m s^{-1}) in convective, stratiform, and non-precipitating updrafts and downdrafts.

buoyancy for updrafts and negative buoyancy for downdrafts. Observationally driven thresholds may not be appropriate for analysis of simulated fluxes. However, some defining threshold value is necessary to filter out all the small and insignificant motions that would dominate the mean conditions without contributing to the relevant transport.

[23] Figure 4 shows the mass flux, defined as $F_{\mathrm{M}} = \overline{\rho}(w - \overline{w})$, where $\overline{\rho}$ is mean air density, w is a vertical velocity and $\overline{w}$ is mean vertical velocity taken over the whole domain. This flux is averaged over the duration of event C and is shown for different draft thresholds $|w_{tr}|$ in D1. Figure 4 (top) shows that most of the convective updraft mass transport is carried by updrafts with a velocity of 1.0 m s^{-1} or greater, but it shows that it is not the case for convective downdraft flux. Convective downdrafts stronger than 1.0 m s^{-1} are responsible for only about 50% of the mass transport, which indicates that a lower threshold should be chosen to account for most of the downdraft mass flux. Results are similar for other simulations (not shown).

[24] In the case of stratiform drafts (Figure 4, middle), both up and down, a threshold closer to 0.1 m s^{-1} captures most of the transport. Following *Zipser* [1977] and *Frederick and Schumacher* [2008] we should expect a weak uplifting (on the order of tens of centimeters per second as shown, for example, in observational studies of *Biggerstaff and Houze* [1991]) in the stratiform region. We see an updraft mass transport that is not negligible compared with the convective updraft transport above 10 km. In the non-precipitating region (Figure 4, bottom) there is a signature of large-scale subsidence, in the form of relatively uniform descent over the depth of the troposphere. In reality, for an event as horizontally extensive as event C, one may expect that much of the subsidence is outside of the forcing domain for the models. The models, on the other hand, have to force subsidence within the domain to balance the convective updrafts, thus possibly suppressing stratiform updrafts. Updraft mass flux in the stratiform and non-precipitating area near the surface are expected to be associated with boundary layer overturning and turbulence.

[25] In Figure 4, which shows results from only one simulation (other simulations appear similar), both convective and stratiform regions are seen to have a downdraft mass flux of similar magnitude, but the distribution of the transport between slow and fast drafts differs. In the convective region the strongest downdrafts (<−1 m s^{-1}) carry half of the transport, and convective downdraft mass flux increases to the melting level, likely resulting from the entrainment of environmental air into the downdrafts and an increase of precipitation from tilting of the convective updrafts. In the stratiform region, the downdrafts responsible for a similar proportion of transport have w <−0.2 m s^{-1}. In both of these regions the maximum of the downdraft flux is collocated with the melting level at about 5 km. In the non-precipitating area, the downdraft flux is uniform and accomplished by compensating subsidence even weaker than in the stratiform region and strong downdraft motions are absent.

[26] To choose our thresholds more systematically, we identify values that capture 90% of the mass transport. Table 1 summarizes the thresholds for which 90% of the vertically averaged mass flux is captured in stratiform and convective regions, averaged over the convective event and over the depth of the troposphere. The mean convective threshold averaged over the simulations for event C for updraft mass transport is close to 0.6 m s^{-1}. For convective downdraft transport the threshold is lower, about −0.3 m s^{-1}. For stratiform area the corresponding updraft and downdraft thresholds are respectively 0.09 m s^{-1} and −0.15 m s^{-1}. For each threshold, resulting mean vertical velocity and fraction

Table 1. Mean Convective and Stratiform Vertical Velocity Threshold ($\overline{w_{tr}}$) Required to Carry 90% of the Updraft and Downdraft Mass Fluxes, Mean Vertical Velocity ($\overline{w}$) in the Drafts Chosen by This Given Threshold, and Fractional Area That They Cover ($\overline{A}$)

	$\overline{w_{tr}}$ (m s^{-1}) Up	$\overline{w_{tr}}$ (m s^{-1}) Down	$\overline{w}$ (m s^{-1}) Up	$\overline{w}$ (m s^{-1}) Down	$\overline{A}$ (%) Up	$\overline{A}$ (%) Down
Convective						
D1	0.64	−0.31	4.00	−1.03	3.00	3.75
D2	0.55	−0.27	3.40	−0.70	2.50	4.00
S2	0.59	−0.30	3.00	−0.90	2.75	3.75
Stratiform						
D1	0.084	−0.17	0.40	−0.40	7.50	13.60
D2	0.095	−0.14	0.25	−0.35	8.75	13.80
S2	0.096	−0.15	0.30	−0.33	10.60	18.00

of the domain covered by the drafts are also listed in Table 1. It is notable that the convective updrafts and downdrafts that carry 90% of the mass flux cover only 3% and 4% of the domain, respectively. Similarly, stratiform updrafts cover 8% of the domain but stratiform downdrafts take up to 15% of the domain area.

[27] Figure 5 shows the contributions to the domain-average fluxes of heat and moisture from updrafts and downdrafts within the convective, stratiform, and non-precipitating regions. The heat fluxes are computed in terms of equivalent potential temperature perturbation $\theta'_e = \theta_e - \overline{\theta_e}$, and the moisture fluxes in terms of total moisture mixing ratio $q'_t = q_t - \overline{q_t}$, where an over-bar denotes an average over the full horizontal extent of the model domain, A_d. Each flux contribution is integrated over the area of updrafts or downdrafts within each region and normalized by A_d and averaged over time. For example, the moisture flux contribution of updrafts within the convective region at one time is given by $A_d^{-1} \int w' q'_t \, \mathrm{d}A$, where $w' = w - \overline{w}$ (note that $\overline{w} = 0$ by virtue of the periodic lateral boundary conditions) and the integral is over the area of updrafts within the convective region. The fluxes of heat and moisture are overwhelmingly dominated by the contributions of updrafts in the convective region and the dependence on vertical wind speed thresholds considerably reduced relative to the dependence of mass fluxes seen in Figure 4.

3.3. Contributions to Mass Transport

[28] To better understand the relative contributions to the total mass flux by the convective and stratiform drafts, we next look at its time evolution over the convective event. Figure 6 illustrates the mass flux vertically averaged over the depth of the troposphere in the three simulations. The difference between the solid and dash-triple-dotted lines shows the contribution from the non-precipitating regions.

[29] During the buildup stage and the peak of the event, most of the updraft mass flux is carried by the convective updrafts in all simulations. Stratiform updraft mass transport becomes comparable in magnitude to the convective mass flux during later stages of the event, after January 23. In particular for S2, after that time the contribution to the total updraft mass flux from stratiform drafts exceeds the convective region's contribution. This is a greater relative contribution than either D1 or D2 simulations, where the stratiform updraft mass flux is typically comparable to the

convective transport. It is likely that the enhancement of stratiform flux in S2 may be partially attributable to gravity waves, which we will assess in a future study.

[30] In the case of downdraft mass fluxes, convective and stratiform regions contribute comparable shares during the buildup and peak of the event. Many past studies [e.g., *Johnson*, 1984; *Houze*, 1989; *Cheng and Yanai*, 1989; *Gray*, 2000] have shown that the stratiform region contribution to total mass flux in MCSs is non-negligible. In this study all three model configurations show very similar behavior. Past the peak of the event, the convective contribution rapidly decreases relative to the stratiform flux. This is particularly clear in S2. Also in S2 there is a strong contribution from the non-precipitating region, especially before onset and after decay of the event. These include the contribution of boundary-layer thermals and shallow convection. Differences between SAM and DHARMA boundary-layer dynamics may be attributable to differences in their dynamical cores.

3.4. Convective Region

[31] Profiles of convective updraft and downdraft mass fluxes are shown in Figure 7. All simulations exhibit a rather similar updraft and downdraft mass flux above the melting level with uniformly stronger fluxes in D1 than in D2 or S2, but D1 and S2 produce very similar fluxes below 6 km making the distinction between impacts from microphysics and dynamics difficult. The drafts in D2 are generally weaker than in the two other simulations, but the peak in the updraft mass flux is located at the same elevation of 4 km as in D1 and S2. The downdraft mass flux peaks at a lower level and is notably stronger below that altitude in S2, indicating possible differences due to dynamics (see also mass fluxes prior to 23.4 in Figure 6c) or possibly to using hail rather than graupel. Across the three simulations the updrafts are very similar below the freezing level in all mass, heat and moisture fluxes.

[32] Draft properties relevant for parameterizations include vertical velocity and buoyancy, which are partitioned into updrafts and downdrafts in the convective region in Figure 8a. The strongest updrafts are found in D1, in which the averaged updraft strength increases up to about 5 km and then stays almost constant up to 12 km. In S2 the average updraft strength increases to a weaker peak at about 5 km and decreases above. D2 has a weaker updraft on average, which increase in strength to about 11 km. The weaker updrafts are likely responsible for the relatively weak fluxes (seen in Figure 7) in D2 with respect to other simulations. Downdraft strengths, on the other hand, show less spread among the simulations, with more or less constant strength over the depth of the troposphere. These results are consistent with the observations of *Zipser and LeMone* [1980], *Lucas et al.* [1994] and *May and Rajopadhyaya* [1999], as well as the numerical simulations of *Xu and Randall* [2001] and *Igau et al.* [1999], where similar updraft and downdraft properties were documented.

[33] Figure 8 also shows the profiles of thermal buoyancy (without water loading, but including the virtual effect) $B = (\theta_v - \overline{\theta_v})/\overline{\theta_v}$, where θ_v is the virtual potential temperature, q_h the water loading (total hydrometeor), and the buoyancy with water loading $B_{wl} = (\theta_v - \overline{\theta_v})/\overline{\theta_v} - q_h$. The over-bars
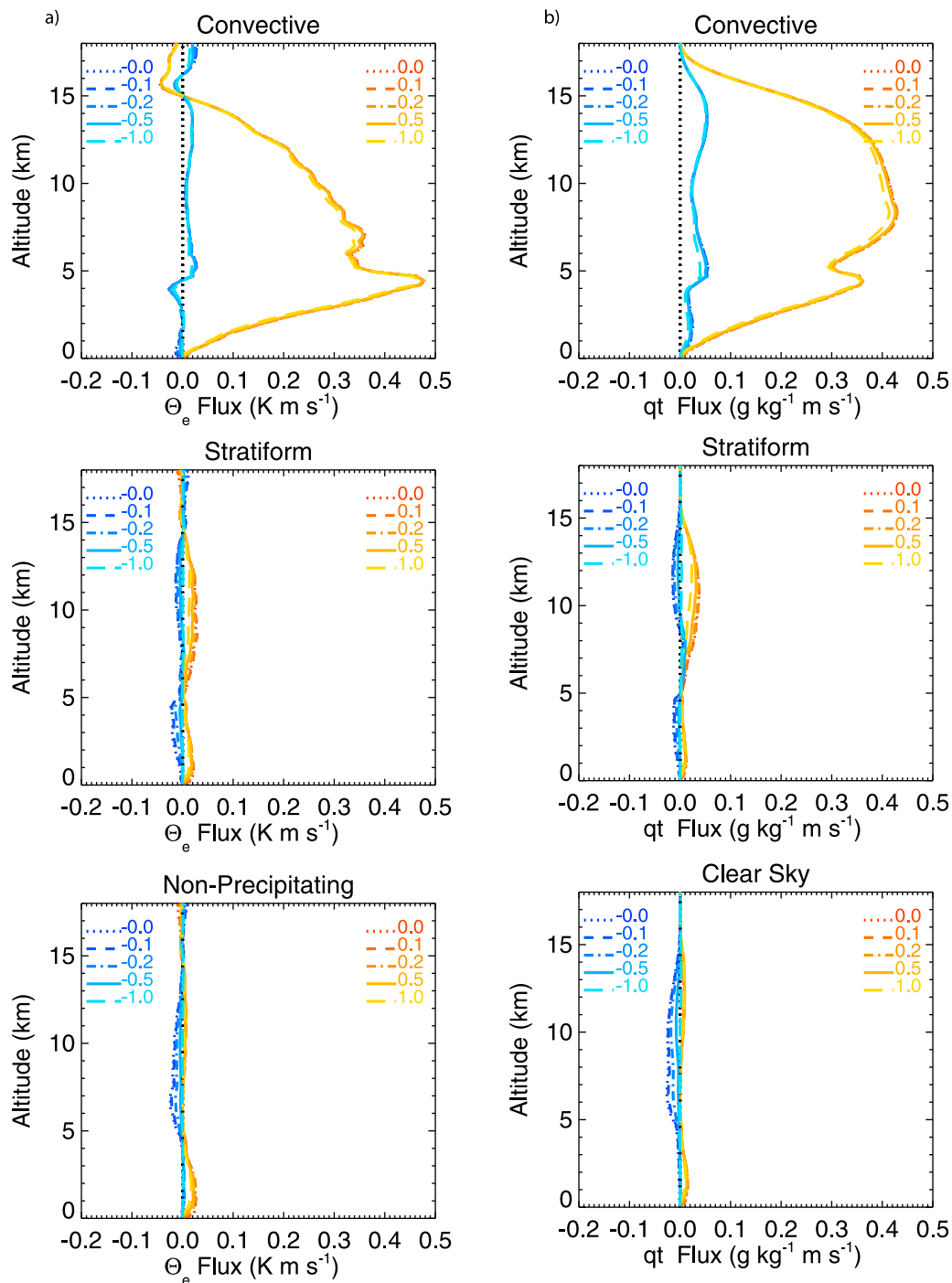
Figure 5. Vertical profiles of equivalent potential (a) temperature flux and (b) moisture flux averaged over the domain during event C shown for D1 simulations with five thresholds on vertical velocity (in units of m s^{-1}) in convective, stratiform, and non-precipitating updrafts and downdrafts. Moisture flux was based on the total water mixing ratio.

signify the domain average. These quantities are shown averaged over the convective event and over the updrafts and downdrafts separately. The average thermal buoyancy in both updrafts and downdrafts is mostly positive. Small buoyancies in updrafts when including water loading have also been confirmed by aircraft observations of deep tropical convection [*Jorgensen and LeMone*, 1989; *Lucas et al.*,

1994; *Wei et al.*, 1998; *Igau et al.*, 1999] and CRM results [*Redelsperger et al.*, 2002].

[34] Water loading (Figure 8c) has a very different vertical distribution in updrafts and downdrafts. In updrafts there is a distinct maximum around 9 km in all the simulations. In downdraft averages there are typically two maxima, one at the surface and another maximum at around 5 km. This melting-level maximum in downdrafts is weaker but
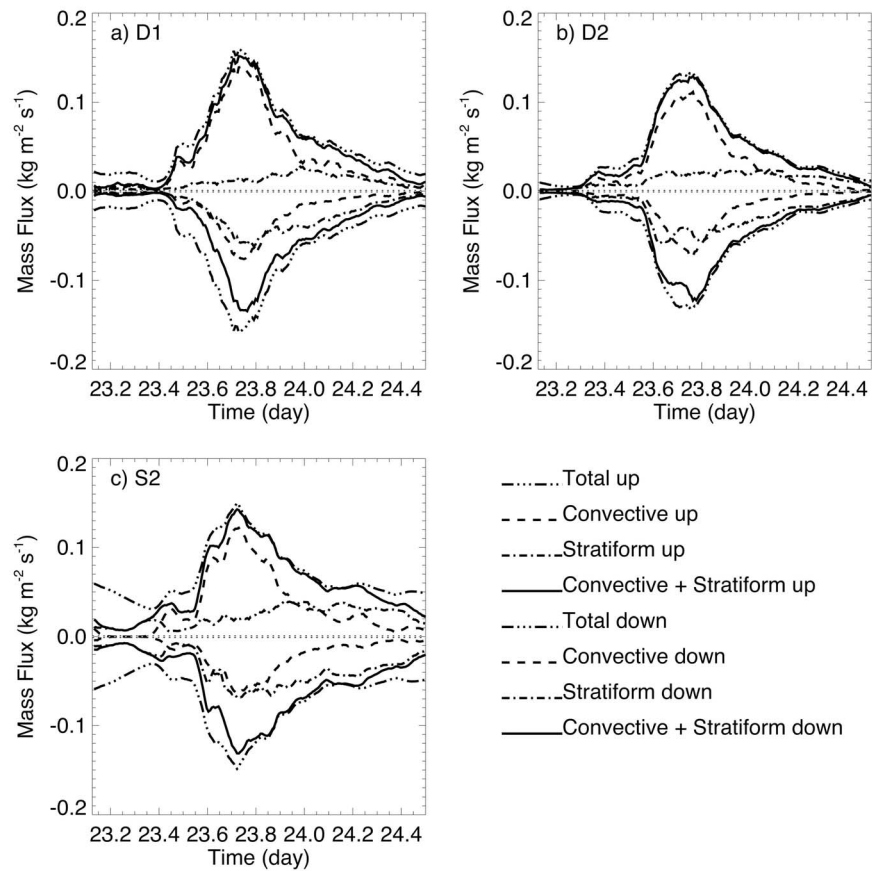
Figure 6. Total, convective and stratiform vertically averaged mass flux in updrafts and downdrafts, shown for (a) D1, (b) D2 and (c) S2. Dash-triple-dotted lines represent the total updraft and downdraft fluxes and solid lines denote the total stratiform and convective updraft and downdraft mass fluxes. Dashed and dash-dotted lines denote the updraft and downdraft convective and stratiform fluxes, respectively. Fluxes are averaged over the lower 17 km of the model domain.

comparable in magnitude to updrafts at the same level. Water loading acts to decrease buoyancy (Figure 8d) resulting in negative buoyancy on average everywhere below 15 km. For the updrafts the impact of water loading is even stronger. At levels below 3 km, the mean updraft buoyancy is negative for all three simulations. Between 3 and 6 km it is positive, and above that it becomes negative with the exception of simulation D2 in which it is positive up
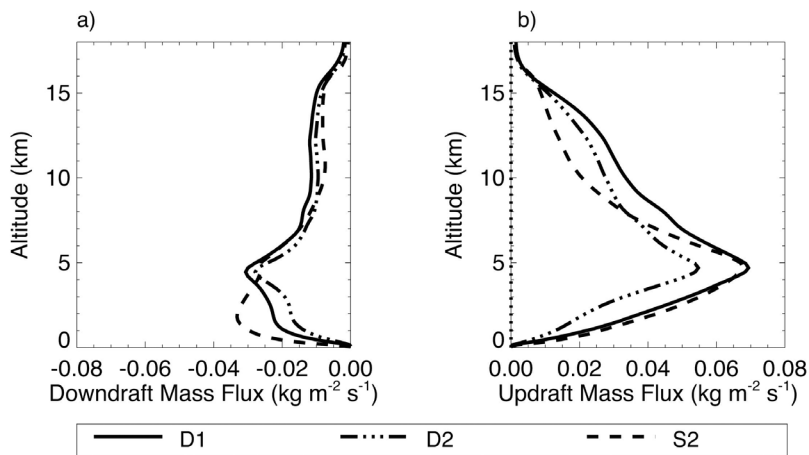

Figure 7. Vertical profiles of convective mass flux in (a) downdrafts and (b) updrafts, averaged over the convective area during event C. Results for D1, D2 and S2 are shown by solid, dash-triple-dotted and dashed lines respectively.
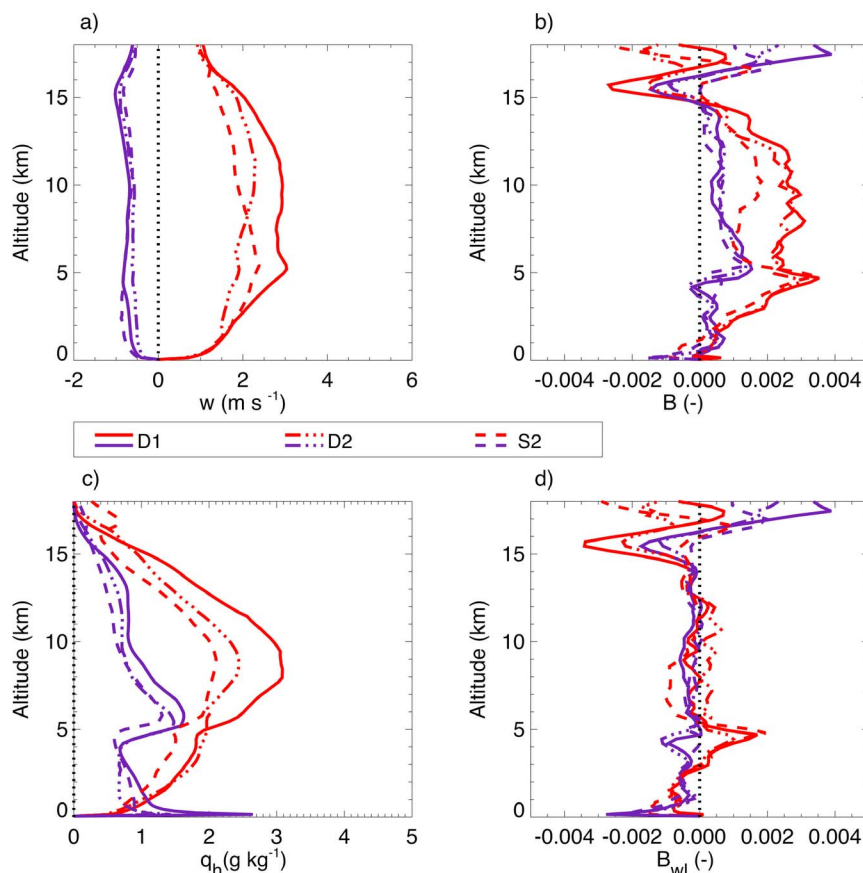
Figure 8. Vertical profiles of (a) convective vertical air velocity, (b) buoyancy without water loading, (c) total hydrometeor mass mixing ratio, and (d) buoyancy with water loading, averaged over the convective areas during event C. Results for D1, D2 and S2 are shown by solid, dash-triple-dotted and dashed lines respectively. Red lines denote properties in updrafts and blue lines in downdrafts.

to 12 km. Upper-level (above 14 km) negative updraft buoyancy is a signature of deceleration, which is likely associated with convection that overshoots. Above 16 km or so, the pairing of negative buoyancy in updrafts and positive buoyancy in downdrafts is indicative of gravity waves.

[35] A key point apparent from this figure is that vertical wind speed is roughly constant in convective downdrafts through much of the troposphere. A second point is that water loading cannot be ignored when computing the buoyancy. Both points are important for parameterizations and are consistent with past literature [e.g., *LeMone and Zipser*, 1980; *Braun and Houze*, 1996; *Xu and Randall*, 2001]. Figure 9 shows the fractional areas of the convective updrafts that are cloudy and downdrafts that are precipitating. Cloudiness is defined by the sum of cloud water and cloud ice mixing ratio exceeding 10^{-6} kg kg^{-1}. As expected, most of the convective updrafts are cloudy. In all three simulations the downdrafts are precipitating below 13 km, where we define the precipitating downdrafts by the sum of all non-cloud hydrometeor (snow, graupel and rain) mixing ratios exceeding 10^{-6} kg kg^{-1}.

[36] The microphysical structure of convective updrafts and downdrafts is shown in Figure 10. The vertical distribution of cloud water (Figure 10a) in updrafts is very similar in the boundary layer for all simulations but above 2 km it strongly increases in one-moment D1, peaking at 5 km and

sharply decreasing above. For D2 and S2 the peaks are smaller and are located slightly higher. There is almost no cloud water in the convective downdrafts. The rainwater mixing ratio profile (Figure 10b) is similar across the simulations; it increases from zero at the surface and peaks at 5 km in updrafts, with the largest peak in D2. In downdrafts the peak is located near the surface.

[37] The total ice mixing ratio profiles (Figure 10c) are fairly comparable in all three simulations, but the partitioning into cloud ice, snow and graupel (Figure 10, bottom) shows large differences. In D1 cloud ice is present at all elevations above the melting level, whereas in D2 and S2 cloud ice is abundant only above roughly 10 km, where cloud droplets freeze homogeneously. The difference is attributable to cloud ice being diagnosed at all levels where there is appreciable snow in the D1 scheme. However, D1 and D2 produce similarly abundant graupel and less snow compared to S2. As noted in section 2, S2 uses a hail formulation for its dense ice, which falls out faster, reducing its convective mixing ratios.

3.5. Stratiform Region

[38] The stratiform region is associated with weak downdrafts, relatively uniform rain and weak mesoscale updrafts (tens of cm s^{-1}) [*Zipser*, 1977] above the melting level. The weak motions make the identification of mass fluxes more
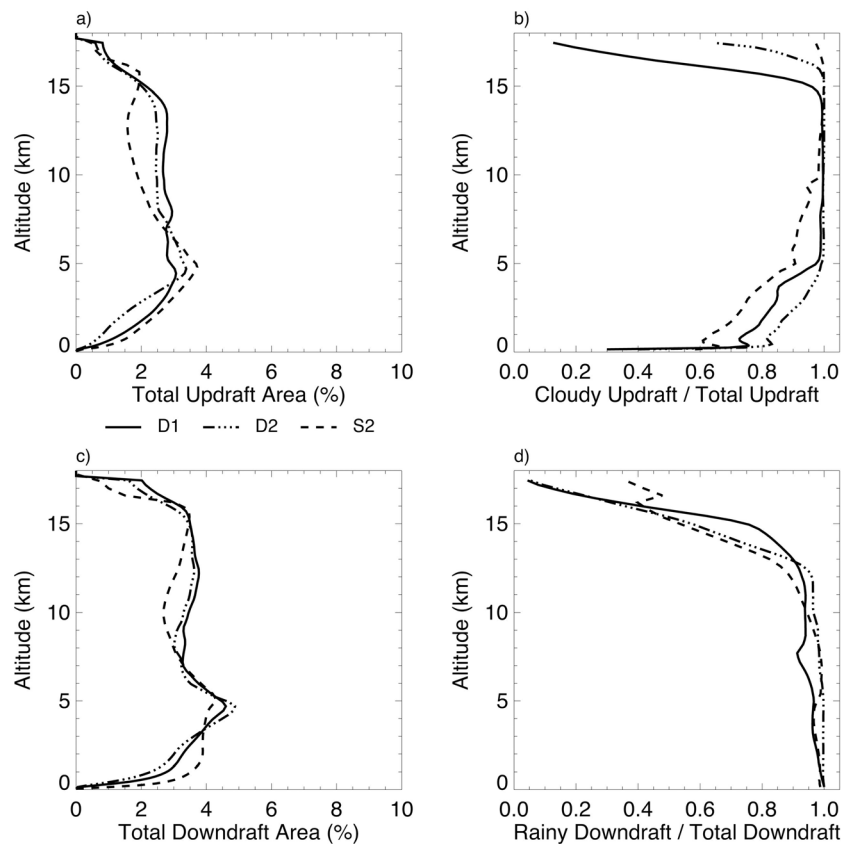
Figure 9. Vertical profiles of the coverage of (a) total convective updrafts, (b) fraction of convective updrafts that are cloudy, (c) fraction of total convective downdrafts, and (d) fraction of convective downdrafts that are rainy. The profiles have been averaged over event C. Results for D1, D2 and S2 are shown by solid, dash-triple-dotted and dashed lines respectively.

difficult than in the case of convective drafts. *Tao and Simpson* [1989] have shown that the major source of the updraft transport in the stratiform region comes from older convective updrafts and small ice detrained into the anvil region. As the anvil sublimes and melts it produces cooling which in addition to evaporation of precipitation into the dry air causes slow descent [*Houze*, 1993, 2004]. A horizontal pressure gradient may additionally be an important source of the mesoscale motions [*Caniaux et al.*, 1995; *Houze*, 2004].

[39] Stratiform mass fluxes found here are shown in Figure 11. Note the different x-axis ranges relative to those used for the convective region (Figure 7). Compared with convective fluxes, a larger portion of the stratiform mass flux is concentrated in the downdrafts, which is similar in magnitude to the convective downdraft flux. There appears to be lower-level overturning in S2 that is not as strong in D1 and D2, but most notable is that mean downdraft mass fluxes exceed updraft mass fluxes in all three simulations, which conflicts with the general expectation that the stratiform region contains a mesoscale updraft above the melting level, as noted above. There may be at least two general explanations for this.

[40] First, the MCS simulated here was larger than the observational domain [cf. *Zhu et al.*, 2012, Figures 3 and 4]. When its active region was contained in the observational domain, observationally derived domain-mean vertical motions reached campaign-wide peaks [*Xie et al.*, 2010,

Figure 8] that were in excess of 25 cm s^{-1} at some elevations. (We note that no such observational constraints are available for the convective and stratiform regions separately.) In the CRM simulations, on the other hand, the domain mean of resolved vertical velocity at all elevations is zero (because the CRMs use periodic lateral boundary conditions), and the effects of large-scale vertical motion are applied directly to potential temperature, water variables, and tracers [*Fridlind et al.*, 2012]. Large-scale vertical motions are also intentionally excluded from our calculations of convective turbulent fluxes in order to analyze results from the convective parameterization point of view. However, a direct comparison with local observations of vertical wind would include the large-scale motion. For instance, Figure 12a shows the domain-average time series of vertical velocity in simulation D1 without the large-scale component and Figure 12b shows the same field with the large scale vertical wind included (the two other simulations are similar). Whereas the resolved motions in the stratiform region are usually net downward, the total vertical wind between 5 and 15 km is usually net upward. Still, the peak convective activity, which happens at day 23.6, forces relatively strong subsidence across the simulation domain. This subsidence in simulations with periodic boundary conditions could be unrealistically large outside of convective regions if it is confined to a smaller area than in reality, as expected here. Aside we note that, to the extent that stratiform
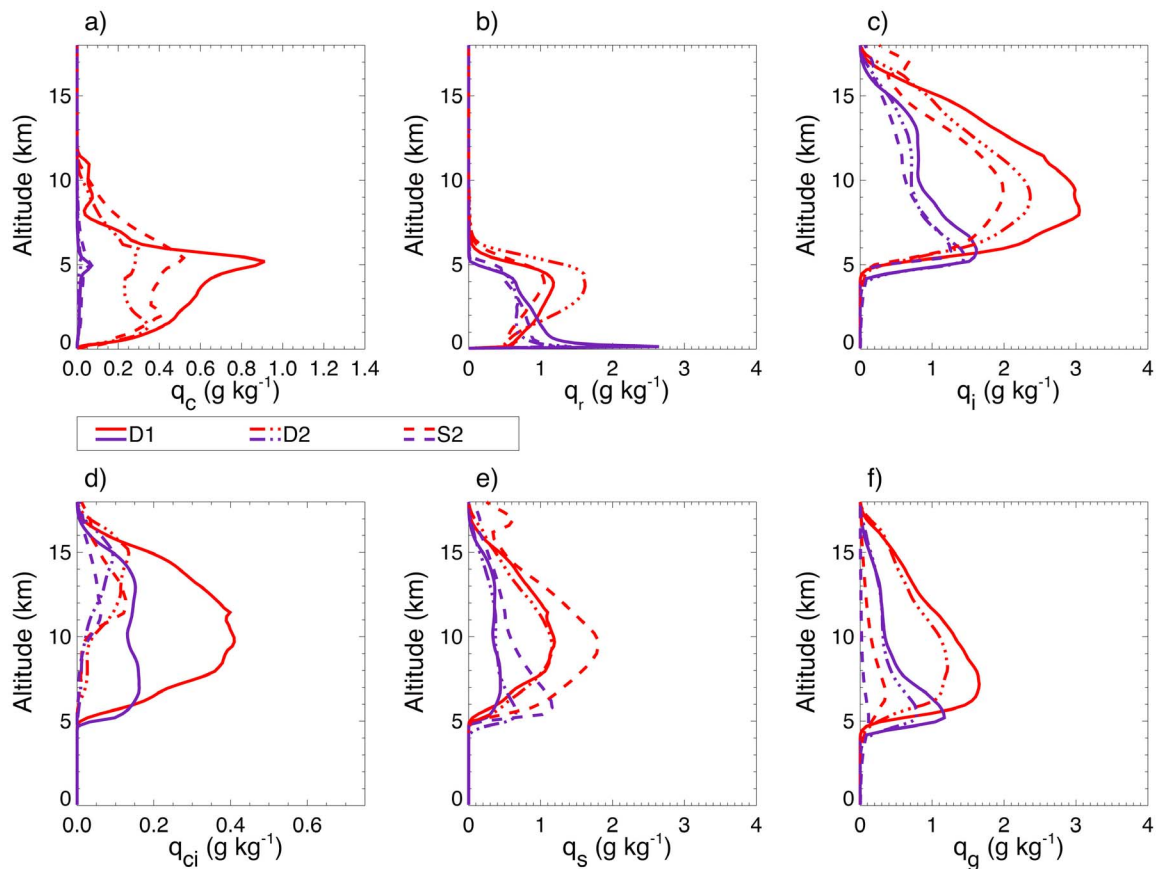
Figure 10. Vertical profiles of hydrometeor mass mixing ratio in the convective region: (a) cloud water, (b) rainwater, (c) total ice water, (d) cloud ice, (e) snow, and (f) graupel (or hail), all averaged over the convective regions during event C. Line patterns and colors as in Figure 8. Note that different x-axis ranges are used in each panel.

updrafts could be suppressed, the same effect would be expected in a GCM so-called superparameterization with embedded periodic CRM calculations [*Randall et al.*, 2003] with similarly imposed large-scale forcings and a similar domain extent (GCM grid cell size).

[41] Second, in this study any CRM column that is not classified as convective and that contains sufficient elevated cloud is considered stratiform. Some of these regions are detached from the main stratiform area or are not part of a large well-defined stratiform area (Figure 1). In addition, an
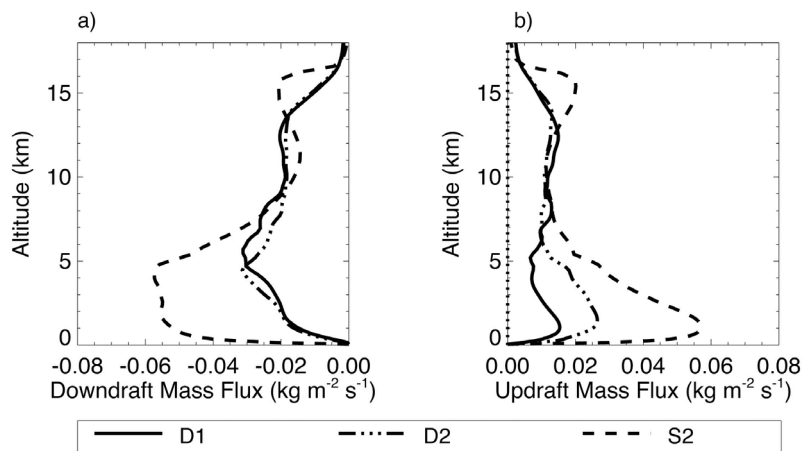

Figure 11. Vertical profiles of stratiform mass flux in (a) downdrafts and (b) updrafts, averaged over the stratiform regions during event C. Results for D1, D2 and S2 are shown by solid, dash-triple-dotted and dashed lines respectively.
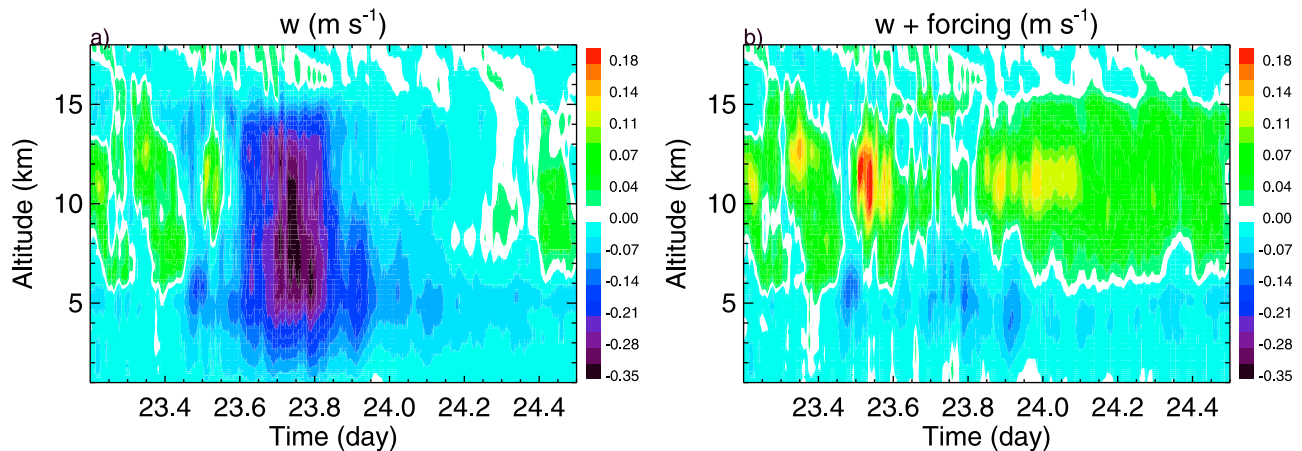
Figure 12. Time series of mean vertical velocity in stratiform region in simulation D1 (a) without large-scale vertical wind and (b) with large-scale vertical wind. Small positive values are shown in white to emphasize the transition from downward to upward motion.

objective of the *Steiner et al.* [1995] algorithm used here is to associate stratiform regions with a pronounced bright band, which could exclude transition regions that may contain detrained buoyancy [e.g., *Yuter and Houze*, 1995] but are also difficult to objectively discern [cf. *Biggerstaff and Houze*, 1993] and are likely less systematically organized in tropical systems [cf. *Mapes and Houze*, 1992]. Thus, mean motions in the stratiform region analyzed here are not directly comparable with the concept of an organized stratiform updraft that applies to a large contiguous stratiform region.

[42] The average vertical air velocities in Figure 13a show weak, rather vertically uniform downdrafts and weak updrafts. There are no significant intensity differences among the simulations. According to *Morrison et al.* [2009] mesoscale updrafts at midlevels are stronger with a two-moment than with a one-moment microphysics scheme in simulations of a mid-latitude squall line. No such trend is evident in these simulations of tropical monsoon convection. Stratiform downdrafts have mostly negative or neutral thermal buoyancy (Figure 13b) except between 5 and 11 km in D2 and S2. Stratiform updrafts generally maintain positive or near-neutral thermal buoyancy in the mid-troposphere, but negative buoyancy near the tropopause and below the melting level for D1 and S2. Similar results were shown in *Gray* [2000].

[43] Water loading in stratiform updrafts and downdrafts (Figure 13c) is the greatest in D1, and similar in D2 and S2. When the water loading is included in the buoyancy (Figure 13d), nearly all stratiform drafts are negatively buoyant, with the exception of downdrafts near the tropopause, consistent with gravity-wave motions there. Aside we note that as shown in *Xu and Randall* [2001], the strongest updrafts throughout the troposphere do have positive buoyancy (not shown). Comparing Figures 8 and 13, the microphysical scheme evidently plays a much greater role in the water loading of drafts in the stratiform region than in the convective region.

[44] Figure 14 shows the fraction of stratiform updrafts that are cloudy and stratiform downdrafts that are precipitating. Similar to the convective cloudiness shown in Figure 9, most

of the stratiform updrafts above 5 km are cloudy. The stratiform updrafts are more abundant in the upper part of the domain and contain mostly cloud ice. In S2 there are also updrafts below the melting line that are associated with near-surface eddies. Nearly all stratiform downdrafts are precipitating below 9 km.

[45] In terms of microphysical properties, cloud water and rain are seen in Figure 15 to be much reduced in the stratiform region for updrafts and downdrafts relative to the convective region. Most condensed water in this region is in the form of ice, and graupel or hail is the least abundant. Most of the cloud ice in the simulations with two-moment schemes is located in the upper troposphere, whereas D1 produces a large amount of cloud ice from the melting level updraft as in convective region. As for stratiform snow, the simulations have similarly shaped vertical profiles for updrafts (peak at 10 km) and downdrafts (peak at 5–6 km) but with different magnitudes. The least amount of snow is seen in D2 in updrafts as well as downdrafts. The total ice is approximately distributed as follows: in simulation D1 there is 30% cloud ice, 60% snow, and 10% graupel; in simulation D2 there is 5–10% cloud ice, 80% snow, and 10–15% graupel; and in S2 the distribution is 10% cloud ice, and 90% snow (no hail). Simulation D1 has the greatest fraction of cloud ice and also the greatest cloud and snow ice path owing in part to the 1-moment scheme's gamma and log-normal particle size distribution assumptions, which lead to high number concentrations that limit snow particle size and associated stratiform snow radar reflectivity shown in *Varble et al.* [2011]. In D1 the division between cloud ice and snow is also diagnostic [*Grabowski*, 1999, equation A.7]. In this formulation, a leading portion of combined cloud ice and snow is always assigned to the cloud ice mode, resulting in greater cloud ice between 5 and 10 km heights.

[46] Comparing Figures 10 and 15, it is apparent that stratiform outflow properties are related to convective properties. Figure 16 shows the ice water path of each type of hydrometeor type in the stratiform versus the convective regions. There is almost as much cloud ice in the stratiform regions as in the convective regions, with an average ratio of 0.9. Cloud ice falls slowly, and is thus readily advected from
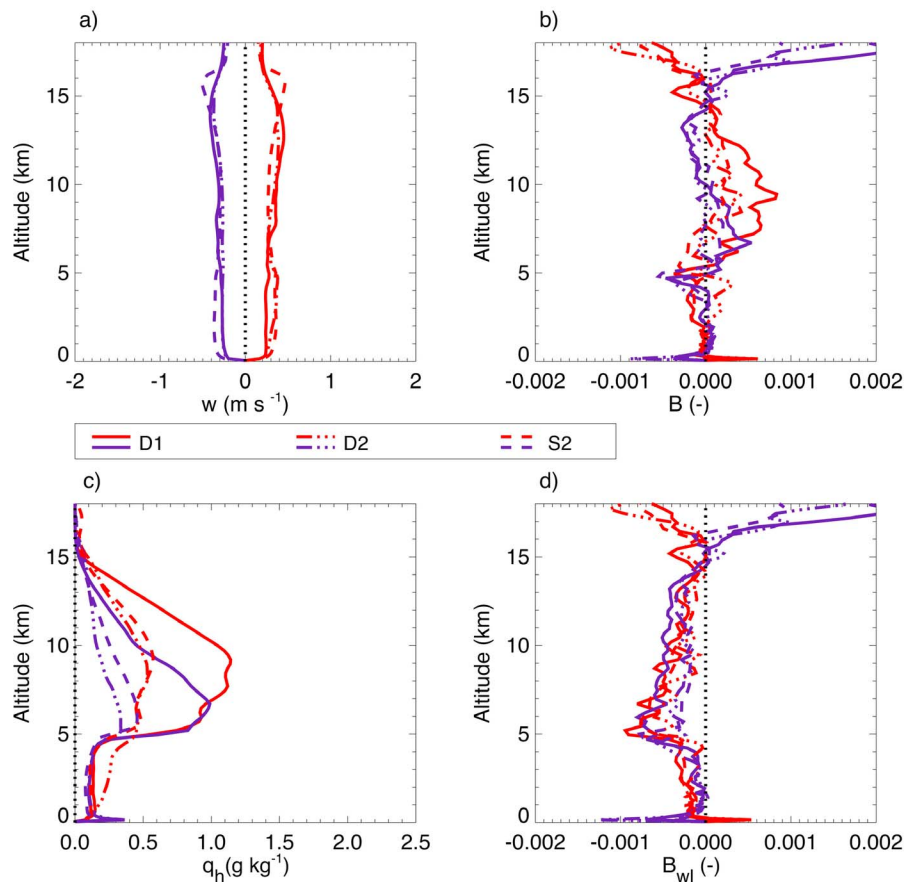
Figure 13. Vertical profiles of (a) stratiform vertical air velocity, (b) buoyancy without water loading, (c) total hydrometeor mixing ratio and (d) buoyancy with water loading, averaged over the stratiform areas during event C. Line patterns and colors as in Figure 8.

convective to stratiform regions. D2 and S2 stratiform regions have respectively about one-third and one-fourth of the snow loading of the convective regions, but in D1 it is close to nine-tenths, a difference that is presumably driven by differing microphysics. The ratio of graupel loadings in the stratiform and convective regions is small (roughly 0.09). Such low ratios are consistent with graupel forming in the strongest updrafts of the convective region and falling out efficiently before being advected into the stratiform regions.

3.6. Cold Pools

[47] Cold pools are typically generated by individual convective downdrafts within the MCS. They expand at the surface, merge with other cold pools, and spread under the MCS. Warmer environmental surface air is displaced updraft by the spreading cold pool outflow and may reach the level of free convection [e.g., *Ross et al.*, 2004]. Cold pools trigger the new convection and thereby impact the organization and propagation of the entire MCS. For these reasons cold pools should be represented in large-scale models. A wake model of cold pools was developed by *Grandpeix and Lafore* [2010] and implemented in the French Laboratoire de Meteorologie Dynamique zoom (LMDZ) model by *Rio et al.* [2009]. Main difficulties of such a parameterization include two-way interaction with the convective parameterization

and realistic representation of the cold pool properties [*Rio et al.*, 2009]. At a minimum the latter could possibly be improved through CRM analysis.

[48] In order to study properties of cold pools such as their size, growth rate, vertical extent and decay, it is necessary to define cold pool boundaries. Since there should be a sharp gradient of temperature at the edge of a cold pool, a temperature drop could be used as a threshold parameter. Because cold pools are gravity currents, perhaps the most appropriate property (according to *Tompkins* [2001]) defining them is their buoyancy acceleration which can be computed using the virtual potential temperature. *Tompkins* [2001] chose $B_g \equiv g\theta_v'/\theta_v = -0.005$ m s^{-2} to define cold pools in his study of CRM results. However in our case this particular value is not suitable (not shown). The utility of a buoyancy acceleration threshold depends not only on the specifics of the simulated case but also on the numerical representation of the mixing processes within the boundary layer.

[49] Here we find that the virtual potential temperature perturbation, $\theta_v' = \overline{\theta_v} - \theta_v$, is more effective than buoyancy acceleration in locating cold pools edges. We use an ad hoc value of $\theta_v' = -1.0$ K to define cold pools, and compute mean cold pool virtual potential temperature perturbation for all the points where the threshold is exceeded. The evolution of
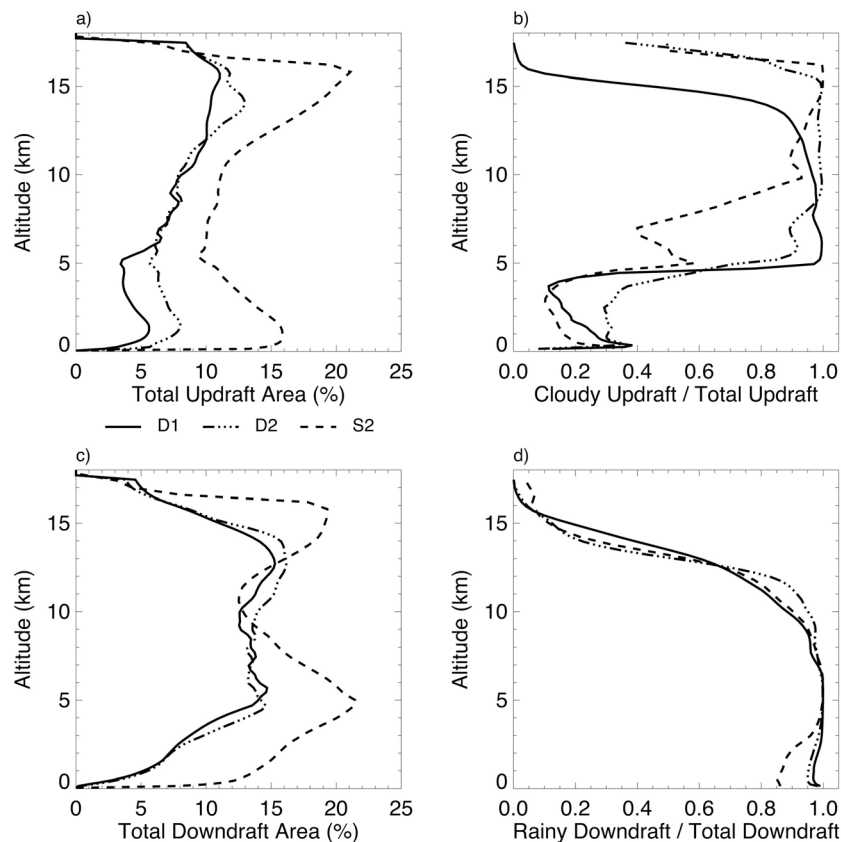
Figure 14. Vertical profiles of the coverage of (a) total stratiform updrafts, (b) fraction of stratiform updrafts that are cloudy, (c) fraction of total stratiform downdrafts, (d) and fraction of stratiform downdrafts that are rainy. The profiles have been averaged over event C. Line types as in Figure 9.

mean and minimum values of cold pool θ_v' are shown in Figure 17a. The minimum values vary across the simulations in terms of amplitude, showing that S2 produces stronger cold pools than both D1 and D2. Aside we note that the mean values are not independent of the θ_v' threshold chosen. There is also a significant variability of the timing of the peak of cold pool surface area (Figure 17b). The cold pool area increases rapidly at about 23.6 (about 15Z on January 23). D2 has a notably weaker and slower cold pool production than either D1 or S2. In D2 the cold pools cover a much smaller area. The main peak of the cold pool activity in D2 also occurs approximately 6 hours after the peak in S2. Furthermore, the non-negligible differences in convective downdraft mass flux below the melting level shown in Figure 7a are positively correlated with cold pool strength. The downdraft mass flux is also related to the θ_v' anomaly, indicating that Figures 17a and 7a are qualitatively consistent.

[50] *Morrison and Milbrandt* [2011] reported that the characteristics of CRM-simulated cold pools are sensitive to dense ice properties in two-moment microphysics schemes. Here simulation S2 with hail exhibits stronger cold pools than D2 with graupel, qualitatively consistent with past results [*Morrison and Milbrandt*, 2011; *Van Weverberg et al.*, 2012]. *Van Weverberg et al.* [2012] also demonstrated that single-moment schemes may produce smaller raindrops and greater evaporation rates and two-moment schemes may produce larger graupel or hail particles owing to size sorting, qualitatively consistent with stronger cold

pools in D1 than D2 here. However, it appears that cold pool properties could also be affected by CRM dynamics. For instance, S2 exhibits notably greater draft fluxes during quiescent times (before 23.4 and after 24.3 in Figure 6) and in the stratiform region below 5 km (Figure 11) than either D1 or D2, differences that are also qualitatively consistent with greater downdraft fluxes in convective regions below 5 km and perhaps stronger cold pools. Regardless of the combined causes of large simulated cold pool differences, Figure 17c indicates that the near-surface q_v anomaly is similar across developed cold pools (e.g., during 23.7–23.8), whereas potential temperature perturbation differences (Figure 17d) correlate with virtual potential temperature differences, a result that may be relevant for parameterization.

4. Statistical Relationships Involving Convective Updrafts and Downdrafts

4.1. Hydrometeor Loading in Convective Downdrafts Versus Updrafts

[51] In convective parameterizations, the number of parameters available to describe the sub-grid scale effect of clouds is limited. Thus small-scale phenomena have to be presented in terms of averaged effect. As already mentioned, the existence of stratiform regions is closely related to processes happening in convective updrafts, in particular the production and distribution of ice hydrometeors. It may therefore be useful to seek robust relationships between
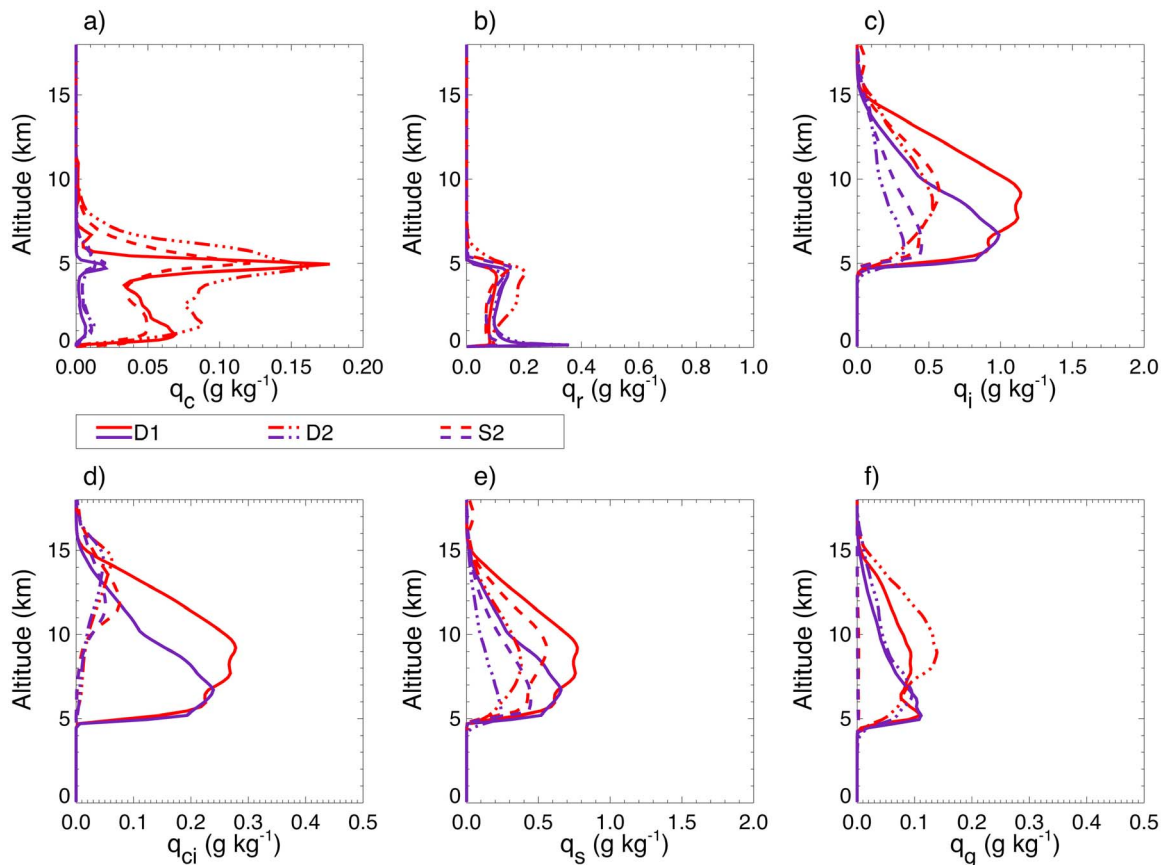
Figure 15. Vertical profiles of hydrometeor mass mixing ratio in the stratiform region: (a) cloud water, (b) rainwater, (c) total ice water, (d) cloud ice, (e) snow, and (f) graupel (or hail), all averaged over the stratiform areas during event C. Line patterns and colors as in Figure 8. Note that different x-axis ranges are used in each panel.

the properties of convective updrafts and downdrafts, for instance.

[52] Figure 18 shows the relationship of convective downdraft and updraft ice water path for different ice hydrometeor types. On average the ratio of ice in convective downdrafts to the ice mixing ratio in the convective updrafts is about 0.5 independent of hydrometeor type across all simulations. Thus, assuming the bulk of downdraft ice mass is generated in updrafts, roughly half of the updraft ice mass is detrained, diluted, melted or evaporated, which may be related to a evaporation efficiency for the convective region.

4.2. Convective Mass Flux Versus Convective Coverage

[53] A comparison of Figures 3 and 6 suggests that updraft and downdraft mass fluxes are correlated with convective areas, at least during the onset of event C. Figure 19a shows that this is a roughly linear correlation which can be physically interpreted as indicating that the vertical air velocity in the updrafts and downdrafts does not vary substantially among the simulations, at least relative to the variability in the mass fluxes themselves. However, a degree of hysteresis appears in both types of drafts (more obvious in the updrafts than in the downdrafts) insofar as the individual points do not randomly fall around the fitted line. Rather, they fall along a coherent loop, for which the right branch in updrafts and left branch in downdrafts marks the buildup of the

convective event (higher fluxes per convective area) and the opposite branches correspond to the decay phase of the event. During buildup of the event, the drafts responsible for the updraft mass flux are stronger, whereas during the decay phase of the convection, as the convective available potential energy (CAPE) has been depleted, the drafts covering the same area are weaker. In other words, for the same mass flux strength, the drafts cover a larger area during the decay phase.

[54] The convective coverage versus updraft or downdraft mass flux is seen in Figure 19a to be similar for D1 and S2, but smaller in D2, consistent with weaker mass fluxes (Figure 7), weaker mid-level drafts (Figure 8), and weaker cold pools (Figure 17). Since D1 and D2 have the same dynamic formulation and D2 and S2 have more similar microphysics schemes, it is likely that the weaker convective flux per convective area in D2 seen in Figure 19a is related to the details of microphysics, the interaction between dynamics and microphysics, or both.

4.3. Convective Mass Flux Up Versus Mass Flux Down

[55] In large-scale models with convective parameterizations based on mass flux closure, it is often assumed that the downdraft mass flux is a fraction of updraft mass flux [e.g., *Raymond et al.*, 2003; *Stensrud*, 2007; *Raymond et al.*, 2009]. Typically this fraction is assumed to be constant
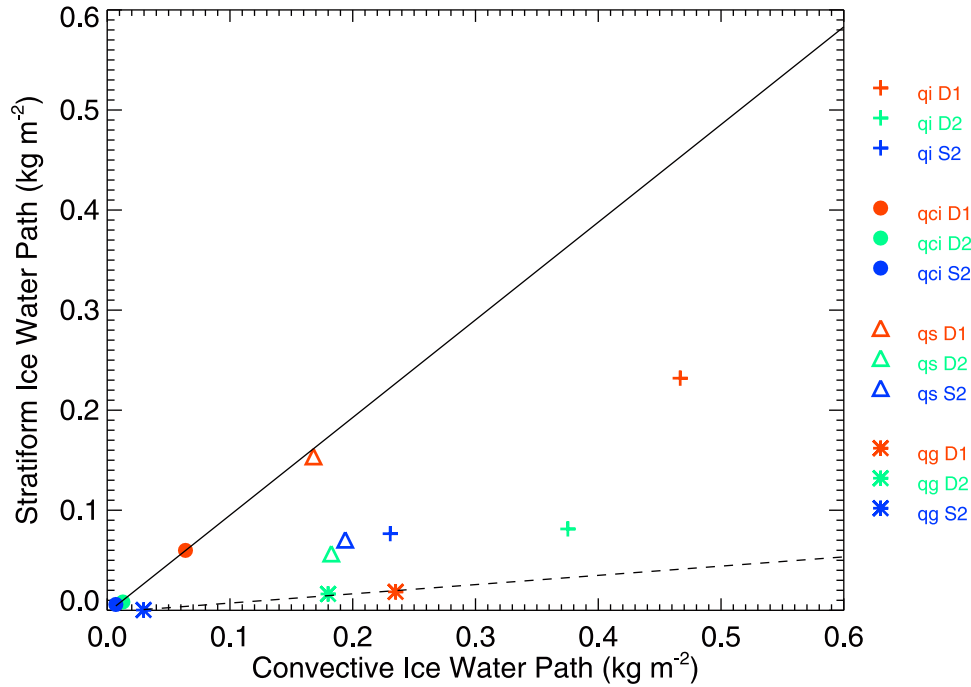
Figure 16. Ice water paths of total ice (plus sign), cloud ice (circle), snow (triangle) and graupel or hail (asterisk) in the stratiform regions versus that in the convective regions, averaged over the stratiform and convective regions, respectively during event C. The least-squares linear fit to cloud ice water paths yields an average ratio between stratiform and convective ice water paths of 0.9 (solid line). The fit to graupel water paths yields a ratio of 0.09 (dashed line).

between 0.25 and 0.5 [*Johnson*, 1976; *Del Genio and Yao*, 1988; *Zhang and McFarlane*, 1995; *Ye et al.*, 1998], though the ratio has been parameterized in terms of physical properties like relative humidity [*Kain et al.*, 2003]. In a study of non-squall-line, slowly moving clusters observed during GATE, *Zipser et al.* [1981] found that the downdraft mass flux was about half of the updraft mass flux up to 3 km.

[56] Downdraft versus updraft convective mass fluxes are shown in Figure 19b. During the event C, all simulations exhibit a relatively linear relationship between the updraft and the downdraft mass fluxes, and the convective downdraft mass flux is about 0.5 to 0.6 of the updraft mass flux. Aside we note that this does not violate mass flux conservation since we only look at the convective region (mass conservation is satisfied over the entire domain). This relationship persists in simulations throughout the active monsoon period illustrated in Figure 3 (not shown).

[57] The ratio of downdraft to updraft mass flux (M^-/M^+) in the convective region can be physically interpreted in terms of an evaporation efficiency by starting with the potential temperature equation,

$$\frac{D\theta}{Dt} = \frac{L_v}{c_p \Pi}(C - E) + \frac{Q_{\mathrm{RAD}}}{c_p \Pi} \qquad (1)$$

where L_v is the latent heat of vaporization, c_p is the specific heat of air at constant pressure, Π is the Exner function, and C, E, and Q_{RAD} are respectively condensation, evaporation and radiative heating rates. We omit melting and freezing under the assumption that they contribute a small net

correction. The left hand side of the above equation may be written as

$$\frac{D\theta}{Dt} = \frac{\partial \theta}{\partial t} + v.\nabla_H \theta + w\frac{\partial \theta}{\partial z} \qquad (2)$$

where here the wind velocity includes large-scales and resolved scales. Under conditions of maritime convection in the tropics, the temperature stays close to the moist adiabat and surface temperatures are stable, so the temporal variation of temperature may be neglected. Also, to first order radiative cooling may be neglected. Horizontal advection is also small since horizontal gradients are weak at large scales [see *Fridlind et al.*, 2012, Figure 3a] as well as convective scales (Figure 8 shows that buoyancy does not add more than 1 K). Thus, the potential temperature equation reduces to a balance between vertical advection and net condensation:

$$c_P \Pi w \frac{\partial \theta}{\partial z} = L_v(C - E). \qquad (3)$$

If motions are decomposed into updrafts and downdrafts, condensation occurs in updrafts, and evaporation occurs in downdrafts, then

$$c_p \Pi \frac{\partial \theta}{\partial z} w^+ = L_v C \quad \text{where} \quad w^+ = H(w)w, \qquad (4)$$

$$c_p \Pi \frac{\partial \theta}{\partial z} w^- = L_v E \quad \text{where} \quad w^- = H(-w)w \qquad (5)$$
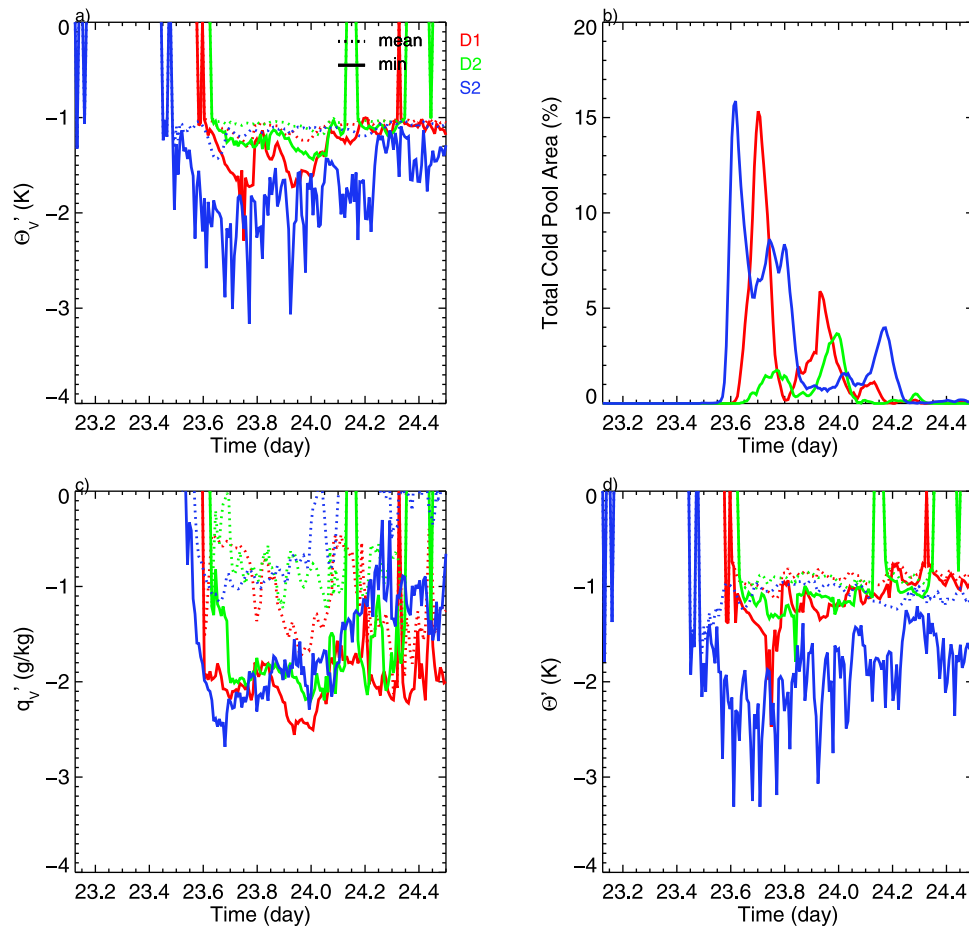
Figure 17. Time series of (a) the mean (dashed lines) and minimum (solid lines) surface virtual potential temperature anomaly in the cold pool regions selected with a θ'_v threshold of -1.0 K, (b) the corresponding cold pool area, (c) water vapor mixing ratio perturbation, and (d) potential temperature perturbation at the surface.

and H is the Heaviside function. After combining these equations and taking into consideration that $\partial\theta/\partial z$ is nearly equal in updrafts and downdrafts (not shown, consistent with weak buoyancy) and that large-scale vertical mass fluxes are small relative to the updraft and downdraft mass fluxes, vertical integration yields

$$\frac{M^-}{M^+} = \frac{\overline{E}}{\overline{C}}, \tag{6}$$

where over-bars denote column total values. Thus a downdraft-to-updraft mass flux ratio of one-half found here can be interpreted as indicating a 50% evaporation efficiency over convective regions for these simulations. As pointed out by *Raymond et al.* [2003], such a proportionality factor is not a constant of nature but rather depends on the state of the environment in which the convection takes place. In simulations under the same environmental conditions, the degree to which this ratio is relatively constant using open boundary conditions might also be considered [e.g., *Zhu et al.*, 2012].

[58] The evaporation efficiency in convective regions may be an interesting parameter to consider more broadly. In sub-Saharan Africa, for instance, even though some of the strongest thunderstorms occur there [*Zipser et al.*, 2006], the surface precipitation is relatively light because of the intense low-level evaporation [*Geerts and Dejene*, 2005]. In such an environment one would expect the evaporation efficiency in convective regions to be closer to unity. Owing to the extremely moist monsoon conditions examined here, an evaporation efficiency of 0.5 could be near a lower limit, which might explain its relative consistency here. The stability of the implied convective evaporation efficiency across these very different simulations warrants further study.

5. Conclusions

[59] In this study we analyzed the properties of three simulations of a mesoscale convective system observed during the TWP-ICE campaign. The properties were viewed from a large-scale modeling perspective. Since models and observations commonly consider convective and stratiform precipitating regions and many GCM parameterizations are based on mass flux closure, we consider primarily the mass fluxes and properties of updrafts and downdrafts in convective and stratiform areas. Our objective is to determine which CRM results are robust and therefore relatively more confidently used for parameterizations development and which are more model-dependent. In a follow-on study we
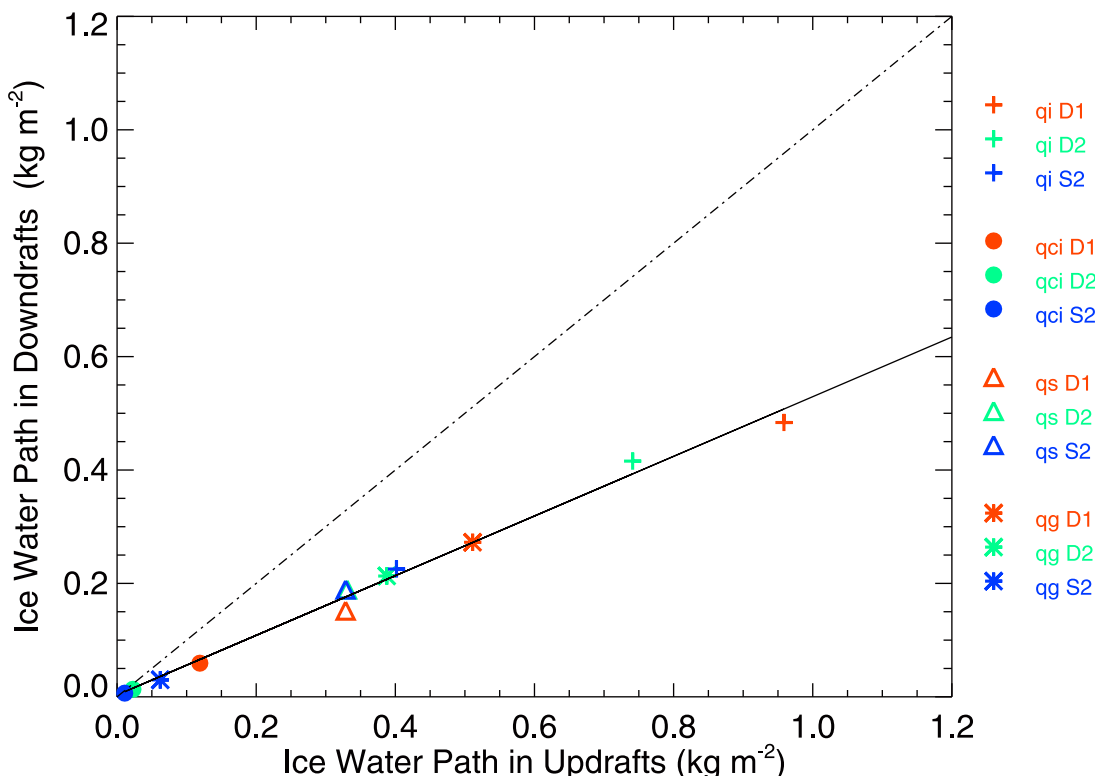
Figure 18. Ice water paths of total ice (plus sign), cloud ice (circle), snow (triangle) and graupel (asterisk) averaged over the updrafts and downdrafts in convective regions during event C. A linear fit through all the points gives a ratio of 0.5 between ice water path in the convective downdrafts and updrafts (solid line). Dash-dotted line shows 1:1 relation.

will use the results here in a comparison with single-column model results.

[60] We took a subset of simulations from a larger CRM intercomparison [*Fridlind et al.*, 2012], namely three 3D simulations that used two different dynamical schemes, and two structurally different microphysical schemes including

two simulations using observation-based aerosol profiles. We also focused on a subset of the simulation time, analyzing the evolution of a single MCS. The simulations roughly reproduced the areal coverage of convective regions during the MCS. We calculated a simulation dependent set of air velocity thresholds to account for 90% of the draft
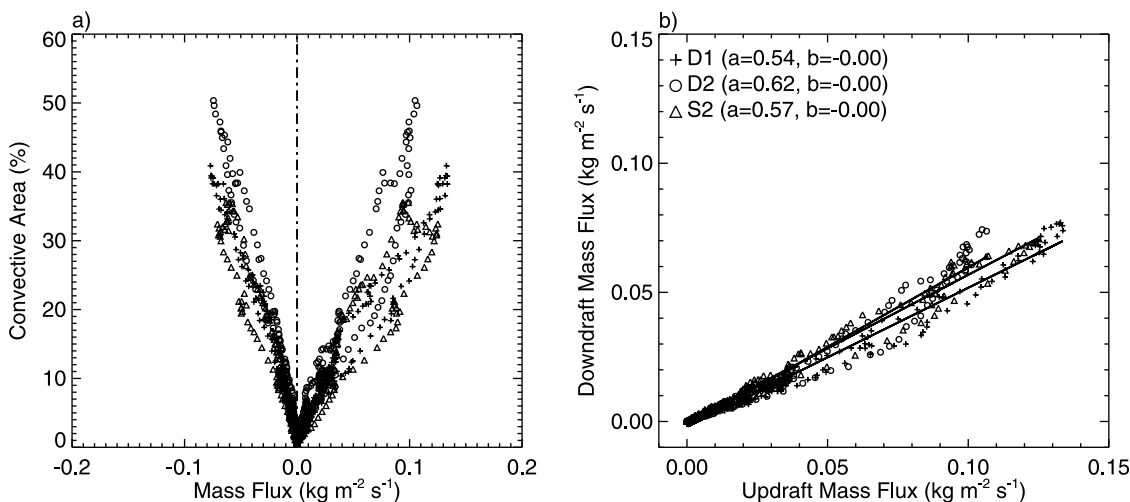

Figure 19. (a) Convective coverage versus vertically integrated convective mass flux in each simulation (D1: plus sign, D2: x symbol, and S2: diamond) and (b) convective updraft versus downdraft mass fluxes with linear fits. Slopes and intercepts are given as a and b in parentheses. Data points are instantaneous values with 10-minute frequency integrated over the depth of the troposphere (from surface to 17 km).

mass fluxes in convective and stratiform regions. There is close agreement of the updraft mass fluxes across the simulations, and convective updrafts do most of the mass transport in the system during the buildup and peak of a major convective event. During the decay phase, the updraft mass flux is divided almost equally between the convective and stratiform regions. In contrast, for downdraft mass flux the convective and stratiform contributions are equally important through all stages of the MCS. The mass flux contribution of the stratiform downdrafts is comparable with that of the convective downdrafts because their greater areal coverage compensates for their weaker air motions.

[61] The simulations show quite similar dynamical properties of convective updrafts. Convective downdrafts, stratiform updrafts, and stratiform downdrafts are nearly vertically uniform in average draft strength in all simulations. We note that mean stratiform updrafts found here could be weak compared with observed mesoscale stratiform updrafts because the simulated MCS was larger than the CRM domain (perhaps forcing descent within stratiform regions) or because the separation algorithm did not require large, contiguous stratiform regions (perhaps including dispersed regions of weak stratiform rain or excluding important transition regions). Substantial differences in cold pool coverage and intensity were found to be attributable to microphysical, and possibly to some extent the dynamical formulation. The greatest difference found among the simulations is in the partitioning of ice among different species, which may depend primarily on microphysical formulation. The greatest microphysical differences were found in the stratiform region. However, a consistent pattern is seen across the simulations insofar as the slowest-falling ice hydrometeor species (cloud ice) is roughly 90% as abundant in the stratiform regions as in the convection region, whereas the fastest-falling hydrometeor species (graupel or hail) is least abundant. In both convective and stratiform regions, downdrafts consistently contain precipitation below about 10 km and updrafts consistently contain cloud ice above the melting level (or at least the homogeneous freezing level in one of the simulations).

[62] Although hydrometeor mass loadings and cold pool properties diverge, several commonalities of convective regions are remarkably consistent across the simulations. First, both convective updraft and downdraft mass fluxes are nearly linearly correlated with convective area. Second, the ratio of ice in convective downdrafts to that in updrafts is about 0.5, independent of ice species. Third, the ratio of downdraft to updraft mass flux is about 0.5–0.6, which can be interpreted as a evaporation efficiency of roughly one-half in convective regions. This ratio surely depends on the environmental conditions and deserves further study. Ultimately, some these findings may lead to improved convective parameterizations in large-scale models.

References

Ackerman, A. S., O. B. Toon, D. E. Stevens, and J. A. Coakley Jr. (2003), Enhancement of cloud cover and suppression of nocturnal drizzle in stratocumulus polluted by haze, *Geophys. Res. Lett.*, *30*(7), 1381, doi:10.1029/2002GL016634.

Arakawa, A., and K.-M. Xu (1992), The macroscopic behavior of simulated cumulus convection and semi-prognostic tests of the Arakawa-Schubert cumulus parameterization, in *Physical Processes in Atmospheric Models: Collection of Papers Presented at the Indo-U.S. Seminar on Parameterization of Subgrid-Scale Processes in Dynamical Models of Medium-Range Prediction and Global Climate, IITM, Pune, India, 6–10 August 1990*, pp. 3–18, John Wiley, New York.

Atlas, D., C. W. Ulbrich, E. A. F. D. Marks Jr., R. A. Black, P. T. Willis, and C. E. Samsury (2000), Partitioning tropical oceanic convective and stratiform rains by draft strength, *J. Geophys. Res.*, *105*(D2), 2259–2267.

Biggerstaff, M. I., and R. A. Houze (1991), Kinematic and precipitation structure of the 10–11 June 1985 squall line, *Mon. Weather Rev.*, *119*(12), 3034–3065.

Biggerstaff, M. I., and R. A. Houze (1993), Kinematics and microphysics of the transition zone of the 10–11 June 1985 squall line, *J. Atmos. Sci*, *50*, 3091–3110.

Braun, S. A., and R. A. Houze (1996), The heat budget of a midlatitude squall line and implications for potential vorticity production, *J. Atmos. Sci.*, *53*(9), 1217–1240.

Bretherton, C. S., and S. Park (2009), A new moist turbulence parameterization in the Community Atmosphere Model, *J. Clim.*, *22*, 3422–3448.

Bringi, V. N., C. R. Williams, M. Thurai, and P. T. May (2009), Using dual-polarized radar and dual-frequency profiler for DSD characterization: A case study from Darwin, Australia, *J. Atmos. Oceanic Technol.*, *26*, 2107–2122.

Brown, J. M. (1979), Mesoscale unsaturated downdrafts driven by rainfall evaporation: A numerical study, *J. Atmos. Sci.*, *36*(2), 313–338.

Bryan, G. H., J. C. Wyngaard, and J. M. Fritsch (2003), Resolution requirements for the simulation of deep moist convection, *Mon. Weather Rev.*, *131*, 2394–2416.

Caniaux, G., J.-P. Lafore, and J.-L. Redelsperger (1995), A numerical study of the stratiform region of a fast-moving squall line. Part II: Relationship between mass, pressure, and momentum fields, *J. Atmos. Sci.*, *52*(3), 331–352.

Cheng, M.-D., and M. Yanai (1989), Effects of downdrafts and mesoscale convective organization on the heat and moisture budgets of tropical cloud clusters. Part III: Effects of mesoscale convective organization, *J. Atmos. Sci.*, *46*(11), 1566–1588.

Collins, W. D., J. Wang, J. T. Kiehl, G. J. Zhang, D. I. Cooper, and W. E. Eichinger (1997), Comparison of tropical ocean–atmosphere fluxes with the NCAR Community Climate Model CCM3, *J. Clim.*, *10*(12), 3047–3058.

Del Genio, A., and J. Wu (2010), The role of entrainment in the diurnal cycle of continental convection, *J. Clim.*, *23*, 2722–2738.

Del Genio, A., and M.-S. Yao (1988), Sensitivity of a global climate model to the specification of convective updraft and downdraft mass fluxes, *J. Atmos. Sci.*, *45*, 2641–2668.

Donner, L. J. (1993), A cumulus parameterization including mass fluxes, vertical momentum dynamics, and mesoscale effects., *J. Atmos. Sci.*, *50*, 889–906.

Fan, J., J. M. Comstock, M. Ovchinnikov, S. A. McFarlane, G. McFarquhar, and G. Allen (2010), Tropical anvil characteristics and water vapor of the tropical tropopause layer: Impact of heterogeneous and homogeneous freezing parameterizations, *J. Geophys. Res.*, *115*, D12201, doi:10.1029/2009JD012696.

Frederick, K., and C. Schumacher (2008), Anvil characteristics as seen by C-POL during the Tropical Warm Pool International Cloud Experiment (TWP-ICE), *Mon. Weather Rev.*, *136*(1), 206–222.

Fridlind, A. M., A. S. Ackerman, J. C. Petch, P. R. Field, A. Hill, G. McFarquhar, S. Xie, and M. Zhang (2010), ARM/GCSS/SPARC TWP-ICE CRM intercomparison study, *NASA Tech. Rep., NASA/TM-2010-215*, 858 pp.

Fridlind, A. M., et al. (2012), A comparison of TWP-ICE observational data with cloud-resolving model results, *J. Geophys. Res.*, *117*, D05204, doi:10.1029/2011JD016595.

Geerts, B., and T. Dejene (2005), Regional and diurnal variability of the vertical structure of precipitation systems in Africa based on spaceborn radar data, *J. Clim.*, *18*, 893–916.

Grabowski, W. (1999), A parameterization of cloud microphysics for long-term cloud-resolving modeling of tropical convection, *Atmos. Res.*, *52*(1–2), 17–41.

Grandpeix, J.-Y., and J.-P. Lafore (2010), A density current parameterization coupled with Emanuel's convection scheme. Part I: The models, *J. Atmos. Sci.*, *67*(4), 881–897.

Gray, M. E. B. (2000), Characteristics of numerically simulated mesoscale convective systems and their application to parameterization, *J. Atmos. Sci.*, 57, 3953–3970.

Guichard, F., et al. (2004), Modeling the diurnal cycle of deep precipitating convection over land with cloud-resolving models and single-column models, *Q. J. R. Meteorol. Soc.*, 130(604), 3139–3172.

Holder, C. T., S. E. Yuter, A. H. Sobel, and A. R. Aiyyer (2008), The mesoscale characteristics of tropical oceanic precipitation during Kelvin and mixed Rossby–gravity wave events, *Mon. Weather Rev.*, 136(9), 3446–3464.

Houze, R. A. (1977), Structure and dynamics of a tropical squall-line system, *Mon. Weather Rev.*, 105(12), 1540–1567.

Houze, R. (1982), Cloud clusters and large-scale vertical motions in the tropics., *J. Meteorol. Soc. Jpn.*, 60, 396–410.

Houze, R. A. (1989), Observed structure of mesoscale convective systems and implications for large-scale heating., *Q. J. R. Meteorol. Soc.*, 115, 425–461.

Houze, R. A. (1993), *Cloud Dynamics*, 573 pp., Academic, San Diego, Calif.

Houze, R. A. (1997), Stratiform precipitation in regions of convection: A meteorological paradox?, *Bull. Am. Meteorol. Soc.*, 78(10), 2179–2196.

Houze, R. A. (2004), Mesoscale convective systems, *Rev. Geophys.*, 42, RG4003, doi:10.1029/2004RG000150.

Igau, R. C., M. A. LeMone, and D. Wei (1999), Updraft and downdraft cores in TOGA COARE: Why so many buoyant downdraft cores?, *J. Atmos. Sci.*, 56(13), 2232–2245.

Johnson, R. H. (1976), The role of convective-scale precipitation downdrafts in cumulus and synoptic-scale interactions, *J. Atmos. Sci.*, 33(10), 1890–1910.

Johnson, R. H. (1984), Partitioning tropical heat and moisture budgets into cumulus and mesoscale components: Implications for cumulus parameterization, *Mon. Weather Rev.*, 112(8), 1590–1601.

Jorgensen, D. P., and M. A. LeMone (1989), Vertically velocity characteristics of oceanic convection, *J. Atmos. Sci.*, 46(5), 621–640.

Kain, J., M. Baldwin, and S. Weiss (2003), Parameterized updraft mass flux as a predictor of convective intensity, *Weather Forecast.*, 18, 106–116.

Keenan, T., K. Glasson, F. Cummings, T. S. Bird, J. Keeler, and J. Lutz (1998), The BMRC/NCAR C-band polarimetric (C-POL) radar system, *J. Atmos. Oceanic Technol.*, 15(4), 871–886.

Khairoutdinov, M. F., and D. A. Randall (2003), Cloud resolving modeling of the ARM summer 1997 IOP: Model formulation, results, uncertainties, and sensitivities, *J. Atmos. Sci.*, 60(4), 607–625.

Khairoutdinov, M. F., S. K. Krueger, C.-H. Moeng, P. A. Bogenschutz, and D. A. Randall (2009), Large-eddy simulation of maritime deep tropical convection, *J. Adv. Model. Earth Syst.*, 1, 15, doi:10.3894/JAMES.2009.1.15.

Kiehl, J. T., J. J. Hack, G. B. Bonan, B. A. Boville, D. L. Williamson, and P. J. Rasch (1998), The National Center for Atmospheric Research Community Climate Model: CCM3, *J. Clim.*, 11(6), 1131–1149.

Krueger, S. K. (1988), Numerical simulation of tropical cumulus clouds and their interaction with the subcloud layer, *J. Atmos. Sci.*, 45(16), 2221–2250.

Lang, S., W.-K. Tao, J. Simpson, and B. Ferrier (2003), Modeling of convective-stratiform precipitation processes: Sensitivity to partitioning methods, *J. Appl. Meteorol.*, 42(4), 505–527.

LeMone, M. A., and E. J. Zipser (1980), Cumulonimbus vertical velocity events in GATE. Part I: Diameter, intensity and mass flux, *J. Atmos. Sci.*, 37(11), 2444–2457.

Lucas, C., E. J. Zipser, and M. A. Lemone (1994), Vertical velocity in oceanic convection off tropical Australia, *J. Atmos. Sci.*, 51(21), 3183–3193.

Mapes, B. E., and R. A. Houze Jr. (1992), An integrated view of the 1987 Australian monsoon and its mesoscale convective systems. I: Horizontal structure, *Q. J. R. Meteorol. Soc.*, 118, 927–963.

Mapes, B. E., and J. Lin (2005), Doppler radar observations of mesoscale wind divergence in regions of tropical convection, *Mon. Weather Rev.*, 133(7), 1808–1824.

Matson, R. J., and A. W. Huggins (1980), The direct measurement of the sizes, shapes and kinematics of falling hailstones, *J. Atmos. Sci.*, 37(5), 1107–1125.

May, P. T., and D. K. Rajopadhyaya (1999), Vertical velocity characteristics of deep convection over Darwin, Australia, *Mon. Weather Rev.*, 127(6), 1056–1071.

May, P. T., J. H. Mather, G. Vaughan, K. N. Bower, C. Jakob, G. M. McFarquhar, and G. G. Mace (2008), The tropical warm pool international cloud experiment, *Bull. Am. Meteorol. Soc.*, 89(5), 629–645.

Morrison, H., and W. W. Grabowski (2011), Cloud-system resolving model simulations of aerosol indirect effects on tropical deep convection and its thermodynamic environment, *Atmos. Chem. Phys.*, 11, 15,573–15,629.

Morrison, H., and J. Milbrandt (2011), Comparison of two-moment bulk microphysics schemes in idealized supercell thunderstorm simulations, *Mon. Weather Rev.*, 139, 1103–1130.

Morrison, H., G. Thompson, and V. Tatarskii (2009), Impact of cloud microphysics on the development of trailing stratiform precipitation in a simulated squall line: Comparison of one-and two-moment schemes, *Mon. Weather Rev.*, 137, 991–1007.

Petch, J. C., A. R. Brown, and M. E. B. Gray (2002), The impact of horizontal resolution on simulations of convective development over land, *Q. J. R. Meteorol. Soc.*, 128, 2031–2044.

Randall, D., M. Khairoutdinov, A. Arakawa, and W. Grabowski (2003), Breaking the cloud parameterization deadlock, *Bull. Am. Meteorol. Soc.*, 84, 1547–1564.

Raymond, D. J., G. B. Raga, C. S. Bretherton, J. Molinari, C. Lopez-Carrillo, and Z. Fuchs (2003), Convective forcing in the Intertropical Convergence Zone of the eastern Pacific, *J. Atmos. Sci.*, 60(17), 2064–2082.

Raymond, D. J., S. Sessions, A. Sobel, and Z. Fuchs (2009), The mechanics of gross moist stability, *J. Adv. Model. Earth Syst.*, 1, 9, doi:10.3894/JAMES.2009.1.9.

Redelsperger, J.-L., D. B. Parsons, and F. Guichard (2002), Recovery processes and factors limiting cloud-top height following the arrival of a dry intrusion observed during TOGA COARE, *J. Atmos. Sci.*, 59, 2438–2457.

Redelsperger, J.-L., et al. (2000), A GCSS model intercomparison for a tropical squall line observed during TOGA-COARE. I: Cloud-resolving models, *Q. J. R. Meteorol. Soc.*, 126(564), 823–863.

Rio, C., F. Hourdin, J.-Y. Grandpeix, and J.-P. Lafore (2009), Shifting the diurnal cycle of parameterized deep convection over land, *Geophys. Res. Lett.*, 36, L07809, doi:10.1029/2008GL036779.

Ross, A. N., A. M. Tompkins, and D. J. Parker (2004), Simple models of the role of surface fluxes in convective cold pool evolution, *J. Atmos. Sci.*, 61(13), 1582–1595.

Smith, P. L. (1984), Equivalent radar reflectivity factors for snow and ice particles, *J. Clim. Appl. Meteorol.*, 23(8), 1258–1260.

Smolarkiewicz, P. K., and W. W. Grabowski (1990), The multidimensional positive definite advection transport algorithm: Nonoscillatory option, *J. Comput. Phys.*, 86(2), 355–375.

Steiner, M., R. A. Houze, and S. E. Yuter (1995), Climatological characterization of three-dimensional storm structure from operational radar and rain gauge data, *J. Appl. Meteorol.*, 34(9), 1978–2007.

Stensrud, D. (2007), *Parameterization Schemes: Keys to Understanding Numerical Weather Prediction Models*, 478 pp., Cambridge Univ. Press, Cambridge, U. K.

Stevens, D. E., and C. Bretherton (1996), A forward-in-time advection scheme and adaptive multilevel flow solver for nearly incompressible atmospheric flow, *J. Comput. Phys.*, 129(2), 284–295.

Stevens, D. E., A. S. Ackerman, and C. S. Bretherton (2002), Effects of domain size and numerical resolution on the simulation of shallow cumulus convection, *J. Atmos. Sci.*, 59(23), 3285–3301.

Tao, W.-K., and J. Simpson (1989), A further study of cumulus interactions and mergers: Three-dimensional simulations with trajectory analyses, *J. Atmos. Sci.*, 46(19), 2974–3004.

Tokay, A., and D. A. Short (1996), Evidence from tropical raindrop spectra of the origin of rain from stratiform versus convective clouds, *J. Meteorol.*, 35(3), 355–371.

Tompkins, A. M. (2001), Organization of tropical convection in low vertical wind shears: The role of cold pools, *J. Atmos. Sci.*, 58(13), 1650–1672.

Toon, O. C. M., T. Ackerman, and K. Santhanam (1989), Rapid calculation of radiative heating rates and photodissociation rates in inhomogeneous multiple scattering atmospheres, *J. Geophys. Res.*, 94(D13), 16,287–16,301.

Van Weverberg, K., et al. (2012), Sensitivity of idealized squall line simulations to the level of complexity used in two-moment bulk microphysics schemes, *Mon. Weather Rev.*, 140, 1883–1907.

Varble, A., A. M. Fridlind, E. J. Zipser, A. S. Ackerman, J.-P. Chaboureau, J. Fan, A. Hill, S. A. McFarlane, J.-P. Pinty, and B. Shipway (2011), Evaluation of cloud-resolving model intercomparison simulations using TWP-ICE observations: Precipitation and cloud structure, *J. Geophys. Res.*, 116, D12206, doi:10.1029/2010JD015180.

Wang, W., and X. Liu (2009), Evaluating deep updraft formulation in NCAR CAM3 with high-resolution WRF simulations during ARM TWP-ICE, *Geophys. Res. Lett.*, 36, L04701, doi:10.1029/2008GL036692.

Wapler, K., T. P. Lane, P. T. May, C. Jakob, M. J. Manton, and S. T. Siems (2010), Cloud-system-resolving model simulations of tropical cloud systems observed during the Tropical Warm Pool-International Cloud Experiment, *Mon. Weather Rev.*, 138(1), 55–73.

Wei, D., A. M. Blyth, and D. J. Raymond (1998), Buoyancy of convective clouds in TOGA COARE, *J. Atmos. Sci.*, 55(22), 3381–3391.

Wu, J., A. D. Del Genio, M.-S. Yao, and A. B. Wolf (2009), WRF and GISS SCM simulations of convective updraft properties during TWP-ICE, *J. Geophys. Res.*, *114*, D04206, doi:10.1029/2008JD010851.

Xie, S., T. Hume, C. Jakob, S. A. Klein, R. B. McCoy, and M. Zhang (2010), Observed large-scale structures and diabatic heating and drying profiles during TWP-ICE, *J. Clim.*, *23*(1), 57–79.

Xu, K.-M., and D. A. Randall (1996), A semi-empirical cloudiness parameterization for use in climate models, *J. Atmos. Sci.*, *53*, 3084–3102.

Xu, K.-M., and D. A. Randall (2000), Explicit simulation of midlatitude cumulus ensembles: Comparison with ARM data., *J. Atmos. Sci.*, *57*, 2839–2858.

Xu, K.-M., and D. A. Randall (2001), Updraft and downdraft statistics of simulated tropical and midlatitude cumulus convection, *J. Atmos. Sci.*, *58*(13), 1630–1649.

Xu, K.-M., et al. (2002), An intercomparison of cloud-resolving models with the atmospheric radiation measurement summer 1997 intensive observation period data, *Q. J. R. Meteorol. Soc.*, *128*, 593–624.

Ye, B., A. D. Del Genio, and K. Lo (1998), CAPE variations in the current climate and in a climate change, *J. Clim.*, *11*, 1997–2015.

Yuter, S. E., and R. A. Houze Jr. (1995), Three-dimensional kinematic and microphysical evolution of Florida cumulonimbus. Part III: Vertical mass transport, mass divergence, and synthesis, *Mon. Weather Rev.*, *123*, 1964–1983.

Zeng, X., W. Tao, T. Matsui, S. Xie, S. Lang, M. Zhang, D. O. Starr, and X. Li (2011), Estimating the ice crystal enhancement factor in the tropics, *J. Atmos. Sci.*, *68*, 1424–1434.

Zhang, G. J. (2009), Effects of entrainment on convective available potential energy and closure assumptions in convection parameterization, *J. Geophys. Res.*, *114*, D07109, doi:10.1029/2008JD010976.

Zhang, G. J., and N. A. McFarlane (1995), Sensitivity of climate simulations to the parameterization of cumulus convection in the Canadian Climate Centre General Circulation Model, *Atmos. Ocean*, *33*, 407–446.

Zhu, P., J. Dudhia, P. R. Field, K. Wapler, A. Fridlind, A. Varble, E. Zipser, J. Petch, M. Chen, and Z. Zhu (2012), A limited area model (LAM) intercomparison study of a TWP-ICE active monsoon mesoscale convective event, *J. Geophys. Res.*, *117*, D11208, doi:10.1029/2011JD016447.

Zipser, E. J. (1969), The role of organized unsaturated convective downdrafts in the structure and rapid decay of an equatorial disturbance, *J. Appl. Meteorol.*, *8*(5), 799–814.

Zipser, E. J. (1977), Mesoscale and convective-scale downdrafts as distinct components of squall-line structure, *Mon. Weather Rev.*, *105*(12), 1568–1589.

Zipser, E. J., and M. A. LeMone (1980), Cumulonimbus vertical velocity events in GATE. Part II: Synthesis and model core structure, *J. Atmos. Sci.*, *37*(11), 2458–2469.

Zipser, E. J., R. J. Meitin, and M. A. LeMone (1981), Mesoscale motion fields associated with a slowly moving gate convective band, *J. Atmos. Sci.*, *38*(8), 1725–1750.

Zipser, E. J., D. J. Cecil, Liu, C., S. W., Nesbitt, and D. P. Yorty (2006), Where are the most intense thunderstorms on Earth?, *Bull. Am. Meteorol. Soc.*, *87* (8), 1057–1071.